Ni^{2+}-assisted catalytic one-step synthesis of Bi/BiOCl/Bi$_2$O$_2$CO$_3$ heterojunction with enhanced photocatalytic activity under visible light

Lingsong Wang [a,c], Huanshun Yin [a,*], Suo Wang [a], Jun Wang [b,*], Shiyun Ai [a]

[a] College of Chemistry and Material Science, Food Safety Analysis and Test Engineering Technology Research Center of Shandong Province, Shandong Agricultural University, 271018 Taian, Shandong, PR China
[b] College of Resources and Environment, Key Laboratory of Agricultural Environment in Universities of Shandong, Shandong Agricultural University, Taian 271018, PR China
[c] Tianjin Key Laboratory of Molecular Optoelectronic Sciences, Department of Chemistry, School of Science, Tianjin University and Collaborative Innovation Center of Chemical Science and Engineering, Tianjin 300072 PR China

ARTICLE INFO

ABSTRACT

Bi/BiOCl/Bi$_2$O$_2$CO$_3$ heterojunction was prepared via one-step hydrothermal process under the synergistic catalysis of Ni^{2+}, where Bi(NO$_3$)$_3$ was employed as Bi source, DMF was used as carbon source and reductant, NiCl$_2$ was adopted as Cl source and co-catalyst. The content of Bi, BiOCl and Bi$_2$O$_2$CO$_3$ can be adjusted by changing the reaction time, temperature, content of DMF and NiCl$_2$. The doping of Bi enhanced the photo-catalytic activity of BiOCl/Bi$_2$O$_2$CO$_3$ under visible-light. Bi/BiOCl/Bi$_2$O$_2$CO$_3$ presented photo-degradation activity for environmental pollutants of rhodamine B, sunset yellow and tetracycline, which were 13.01, 9.40, 1.50 times and 168.38, 10.90, 4.75 times higher than BiOCl and Bi$_2$O$_2$CO$_3$, respectively. The improved photocatalytic activity was ascribed to the sensitized effect of Bi and BiOCl, the surface plasmon resonance effect and the heterojunction structure, which inhibited the recombination of photogenerated electron-hole pairs. The degradation mechanism for rhodamine B was discussed, and the decreased toxicity of the degradation products was demonstrated.

1. Introduction

As a kind of promising technology for environmental pollution restoration, photocatalysis has attracted widespread attentions in the last decades due to the advantages of easy operation, simple instrument, low energy consumption, inexpensive reagent, high efficiency, and environment-friendliness [1–5]. In photocatalysis process, photocatalyst greatly influence the photocatalytic degradation efficiency of pollutants. Thus, the pursuit of excellent photocatalyst will never stop. In particular, there is a great demand for photocatalysts with visible light activity due to their broad-spectrum response to sunlight. The application of photocatalysts with visible light activity can also enhance the effective utilization of sunlight. Among various photocatalysts, semiconductor nanomaterials have received more attentions due to the merits of easy excitation by visible light, low cost and high activity, such as g-C$_3$N$_4$, TiO$_2$, CdS, MXene and ZnO [6–13]. As a new type of semiconductor photocatalyst, bismuth-based nanomaterials have gained much attention based on their superior photocatalytic properties under visible light

irradiation due to their appropriate band gap and hierarchical structure [14]. Bi$_2$O$_2$CO$_3$, a *n*-type of semiconductor with typical Sillén structure, presents a high photocatalysis ability, where [Bi$_2$O$_2$]$^{2+}$ slices are located at the middle of two CO$_3$$^{2-}$ anion layers [15]. Up to now, Bi$_2$O$_2$CO$_3$-based composites have been widely applied in photocatalytic degradation of organic pollutants [16,17]. However, due to the wide band gap (about 3.2–3.5 eV), pure Bi$_2$O$_2$CO$_3$ is mainly excited by ultraviolet light (about 4% of solar energy) [18–20], which greatly limits its application. To conquer this shortcoming, various strategies have been developed, such as metal doping, formation heterojunction structure with other semiconductors, manufacturing defects, etc [21–25].

As a simple solution, the formation of heterojunction has been widely used to improve the light absorption wavelength of semiconductor nanomaterials and to increase the migration rate of photo-generated electrons. BiOCl is a layer structure containing (Bi$_2$O$_2$)$^{2+}$ layer and double Cl$^-$ slabs, anisotropic properties, and internal static electric fields, resulting in high separation efficiency of photogenerated electron-hole pairs [23,26]. Fortunately, BiOCl possesses proper energy band

---

* Corresponding authors.
  E-mail addresses: yinhs@sdau.edu.cn (H. Yin), jwang@sdau.edu.cn (J. Wang).

structure, which allows BiOCl to form a heterojunction structure with $Bi_2O_2CO_3$, increasing the electron migration rate, decreasing the recombination of photogenerated electron-hole pairs and ultimately improving the photocatalytic activity of $Bi_2O_2CO_3$. Thus, $Bi_2O_2CO_3$/BiOCl has been successful synthesized and applied to photocatalytic degradation of methyl orange and tetracycline hydrochloride under simulate sunlight and visible light, respectively [27,28]. Though $Bi_2O_2CO_3$/BiOCl showed photocatalytic activity on methyl orange and tetracycline hydrochloride degradation, the demand for improved photocatalytic activity is still required. Thus, another strategy caught our attention. That is metal element doping. As a semimetal, Bi nanoparticle not only presented an exceeding narrow band gap, but also possessed surface plasmon resonance (SPR) behavior [29]. Therefore, Bi nanoparticles were usually employed to functionalize other bismuth-based photoactive nanomaterials to improve their photocatalytic activity. For instances, $Bi/Bi_2O_2CO_3$ [30], Bi/BiOCl [31,32], Bi/BiOI [33], Bi/Bi_4NbO_8Cl [34], $Bi-Bi_{12}O_{17}Cl_2$ [35], $Bi/Bi_2O_3/Bi_2WO_6$ [36], Bi/Bi_4MoO_9 [37] have been reported with improved photocatalytic activity with Bi nanoparticles modification.

Inspired by those work, we designed a $Bi/BiOCl/Bi_2O_2CO_3$ heterojunction, which was successfully synthesized by one-step hydrothermal method with the in-situ formation of Bi nanoparticle and $Bi_2O_2CO_3$ on BiOCl surface for the first time. Herein, N, N-dimethylformamide (DMF) was employed as carbon source and reducing agent, $NiCl_2$ was used as catalyst for the reduction of Bi^{3+} and Cl source, $Bi(NO_3)_3$ was adopted as Bi source. The content of Bi, BiOCl and $Bi_2O_2CO_3$ could be controlled by varying the hydrothermal reaction time. The prepared $Bi/BiOCl/Bi_2O_2CO_3$ heterojunction presented excellent photocatalytic activity for the degradation of rhodamine B (RhB), sunset yellow and tetracycline under visible light ($\lambda = 420$–780 nm) irradiation.

2. Experimental

2.1. Reagents

$Bi(NO_3)_3.5H_2O$, $NiCl_2.6H_2O$, $Na_2SO_4.10H_2O$, KCl, tetracycline hydrochloride, sunset yellow, RhB were purchased from Aladdin (Shanghai, China). Ethanol and DMF was provided by Tianjin Kaitong Chemical Reagent Co., Ltd.

2.2. Characterization

The morphologies of the prepared nanomaterials were recorded by cold-field emission scanning electron microscope (SEM, Hitachi Regulus 8100, Japan) and high-resolution transmission electron microscope (HRTEM, Tecnai-G2 F20, FEI, USA). The phase constituent and diffraction data were analyzed by X-ray diffractometry (XRD, D/max-2500, $\lambda = 1.5406$ Å, Cu Kα) in the 2θ angles range from 5° to 70° (Smartlab SE, Rigaku, Japan). UV–visible (UV–vis) diffuse reflection spectrum was investigated by a UV–vis spectrophotometer ($BaSO_4$ as reflection standard, UV-2550PC, Shimadzu, Japan). Photoluminescence spectra were obtained from Cary Eclipse fluorescence spectrophotometer (Varian, USA). X-ray photoelectron spectroscopy (XPS) analysis was carried out at Thermo ESCALAB 250XI spectrometer (Thermo Fisher Scientific, USA) with a monochromatized Al Ka ($h\nu$ =1486.6 eV) radiation source and power of 150 W. Electron spin resonance (ESR) spectra of paramagnetic species spin-trapped with 5,5-dimethyl-ʟ-pyrroline-N-oxide (DMPO) were recorded with a JEOL JES-X320 spectrometer (Japan). Photoelectrochemical (PEC) measurement was performed at a CHI832A electrochemical workstation (CHI, Austin, USA) equipped with a 500 W Xe lamp as light source. To eliminate the ultraviolet light, a filter was employed to cut off the light under 420 nm. The traditional three-electrode system was used, where ITO electrode was used as working electrode, saturated calomel electrode was used as reference electrode, and platinum column electrode was used as counter electrode. The ITO electrode was self-made with the electrode area of 0.195 cm^2.

0.1 M Na_2SO_4 solution was employed as an electrolyte. Electrochemical impedance spectroscopy (EIS)was obtained at a CHI660E electrochemical workstation (CHI, Austin, USA) with three-electrode system in 0.5 M Na_2SO_4 solution, where modified glassy carbon electrode was employed as working electrode. Total Organic Carbon (TOC) measurement was performed at Shimadzu TOC-L CPN analyzer (Janpa).

2.3. One-step synthesis of $Bi/BiOCl/Bi_2O_2CO_3$

0.48 g $Bi(NO_3)_3.5H_2O$ was dissolved in 60 mL of 1 M HNO_3 with the aid of magnetic stirring. When transparent solution was obtained, 0.19 g of $NiCl_2.6H_2O$ was further added into the solution and magnetically stirred for 15 min to form a uniform suspension. Then, 10 mL of DMF was introduced into the above suspension and magnetically stirred for another 15 min at room temperature. Subsequently, the suspension was transferred into a 100 mL Teflon lined stainless steel autoclave, which was then incubated at 170 °C for 12 h. After naturally cooled to ambient room temperature, the sediment was collected by centrifugation, and washed several times with deionized water and ethanol. The prepared $Bi/BiOCl/Bi_2O_2CO_3$ was dried in a vacuum oven at 60 °C for 12 h.

For comparison, BiOCl and $Bi_2O_2CO_3$ were also prepared according to previous reports, respectively [20,38]. To prepare BiOCl, 3.88 g Bi $(NO_3)_3.5H_2O$ and 0.47 g NaCl were introduced into 48 mL deionized water with magnetically stirring to obtain a suspension. After that, the suspension was further stirred for 1 h, which was then transferred into a 100 mL Teflon lined stainless steel autoclave and incubated at 160 °C for 24 h. The prepared BiOCl was collected with centrifugation and washed wit deionized water and ethanol for several times. Finally, BiOCl was dried in a vacuum oven at 60 °C for 12 h. To prepare $Bi_2O_2CO_3$, 0.5 g urea was dissolved into 40 mL ethanol with magnetically stirring, and then 2.45 g $Bi(NO_3)_3.5H_2O$ was further introduced into the above solution, which was magnetically stirred for 30 min at room temperature. Afterwards, the obtained suspension was transferred into a 100 mL Teflon lined stainless steel autoclave. After incubation at 200 °C for 2 h, the reactor was cooled to room temperature naturally. The prepared $Bi_2O_2CO_3$ was collected by centrifugation and purified by washing with deionized water and ethanol for several times. Before use, it was dried in a vacuum oven at 60 °C for 12 h.

In addition, BiOCl and $Bi_2O_2CO_3$ were also prepared by adjusting the reaction conditions. In brief, BiOCl and $Bi_2O_2CO_3$ were prepared according to the above procedure except the addition of DMF and $NiCl_2$, respectively. The prepared BiOCl and $Bi_2O_2CO_3$ were labeled as BiOCl-1 and $Bi_2O_2CO_3$-1. The performances for BiOCl-1 and $Bi_2O_2CO_3$-1 were also characterized and listed in Supplementary materials.

2.4. Evaluation of photocatalytic performances

The photocatalytic performances of $Bi/BiOCl/Bi_2O_2CO_3$ were evaluated by degrading three kinds of different organic pollutants, including RhB, sunset yellow and tetracycline. Typically, 50 mg catalyst was dispersed into 40 mL deionized water under ultrasonication for 30 min. Then, 10 mL of 100 ppm organic pollutant aqueous solution was further introduced into the dispersion. After that, the dispersion was transferred into a degradation cell and stirred at room temperature for 60 min to achieve an adsorption-desorption equilibrium. Subsequently, the dispersion was irradiated with visible light originated from a 300 W Xe lamp equipped with a filter, which cut off the light with the wavelength lower than 420 nm. To exclude the effect of the increasing temperature, the degradation cell was equipped with a condensing device. At certain time intervals, 2.0 mL aliquot was sampled from the dispersion, and the catalyst was eliminated by centrifugation. The UV-Vis spectra of the organic pollutants in the supernatant were recorded on UV-2700 UV–visible spectrophotometer (Shimadzu, Japan). The degree of degradation was expressed as C_t/C_0, where C_0 represented the pollutant concentration at dark sorption equilibrium and C_t represented the concentration after each interval [39].
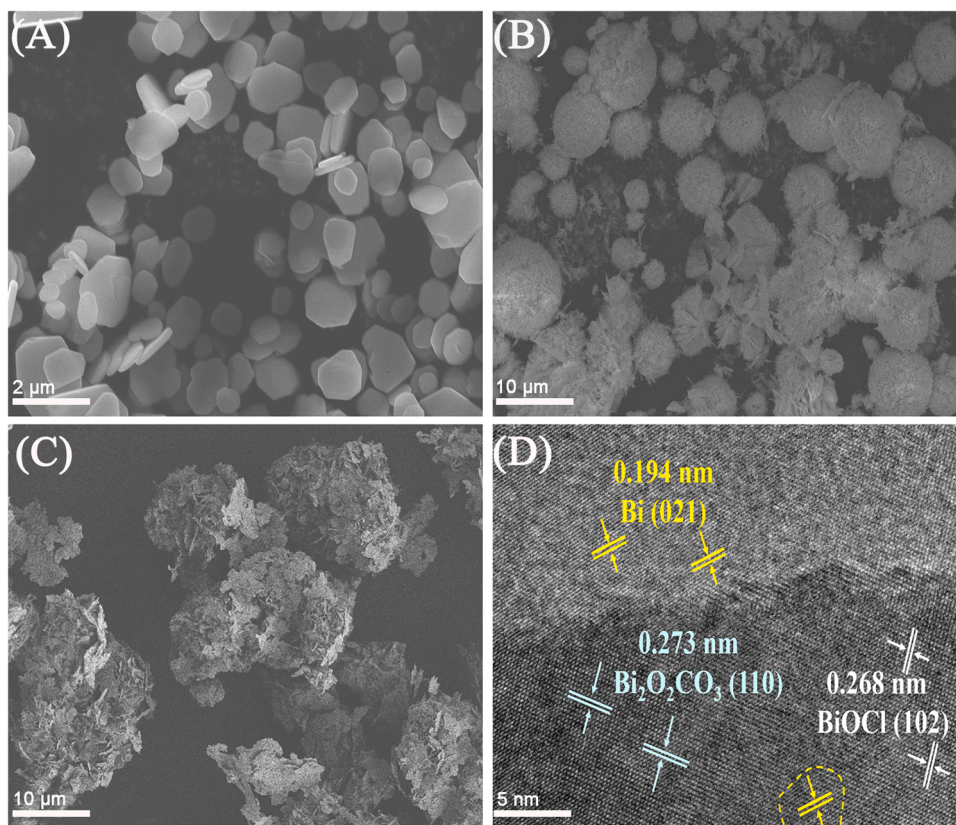
Fig. 1. SEM images of BiOCl (A), $Bi_2O_2CO_3$ (B) and $Bi/BiOCl/Bi_2O_2CO_3$ (C). (D) HRTEM image of $Bi/BiOCl/Bi_2O_2CO_3$.

2.5. Analysis of degrading products of RhB

Agilent 1100-Thermos TSQ Quantum Ultra (LC-ESI-MS) with C18 column (Venusil MP C18 2.1 ×150 mm, 3 μm) was used to determine the intermediates in the degradation process. The chromatographic conditions were as follows. C18 column was eluted with a gradient of 0.1% formic acid in water (A) and acetonitrile (B) at a 0.35 mL/min flow rate and column temperature of 45 °C as follows: 0–1.5 min, 10% of B; 1.5–8 min, 10% of B; 8–10.5 min, 92% of B; 10.5–10.51 min, 10% of B. The analysis of RhB degradation products was performed by direct of the time-dependent degradation solution, diluted with 0.1% formic acid in water with a syringe pump rate of 3 μL/min. The mass spectrometry (m/z 50–1000) was calibrated in positive mode using a solution of sodium formate (10 mM). Other conditions for mass spectra were as follows. Scan type, full scan; Scan mode, Q1MS; Scan time, 0.95 s; Spray voltage, 3300 V; Vaporizer temperature, 450 °C; Sheath gas pressure, 50 bar; Ion sweep gas pressure, 2.0 bar; Aux gas pressure, 15 bar; capillary temperature, 350 °C; collision energy, −10 eV.

3. Results and discussion

3.1. Morphology and structure characterization

The morphology of $Bi/BiOCl/Bi_2O_2CO_3$ was firstly analyzed by SEM, and the results were shown in Fig. 1. $Bi/BiOCl/Bi_2O_2CO_3$ demonstrated an irregular loose spherical block structure formed by the stacking of thin nanosheets (Fig. 1A). The mutual staggered thin nanosheets could provide a large specific surface area and offered more active sites to facilitate the photocatalytic degradation of organic pollutants. The prepared $Bi/BiOCl/Bi_2O_2CO_3$ was also characterized by HRTEM. As seen in Fig. 1B, the clear lattice spacing of 0.268 and 0.273 nm was indexed to the (102) plane of BiOCl and the (110) plane of $Bi_2O_2CO_3$, respectively.
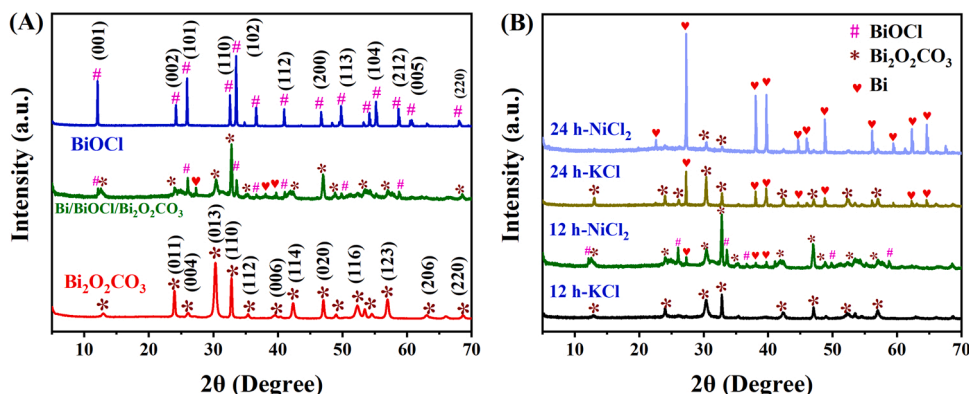

Fig. 2. (A) XRD patterns of BiOCl, $Bi_2O_2CO_3$ and $Bi/BiOCl/Bi_2O_2CO_3$. (B) XRD patterns of the samples prepared with KCl and $NiCl_2$.
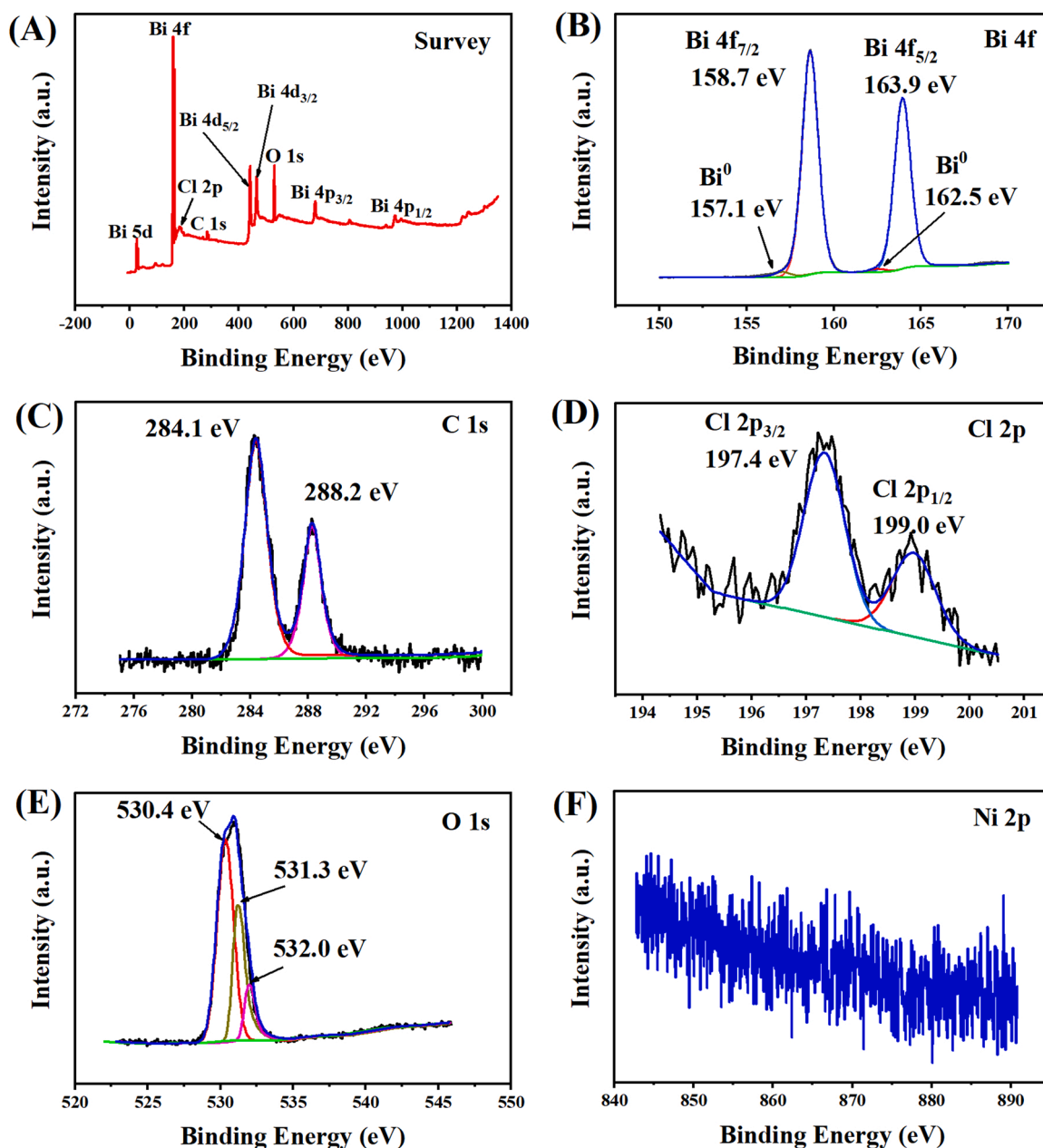
Fig. 3. XPS spectra of Bi/BiOCl/$Bi_2O_2CO_3$. (A) survey spectra, (B) Bi 4f, (C) C 1s, (D) Cl 2p, (E) O 1s and (F) Ni 2p.

Besides, 0.194 nm was corresponding to the (021) plane of Bi. Thus, it could be tentatively proved that Bi, BiOCl and $Bi_2O_2CO_3$ co-exist in the composite, indicating the successful preparation of a ternary composite catalyst of Bi/BiOCl/$Bi_2O_2CO_3$.

The crystallographic and phase structure of the samples were investigated by XRD, and the diffraction patterns were illustrated in Fig. 2. For pure BiOCl, all the diffraction peaks (marked with the symbol of #) were exactly indexed to tetragonal BiOCl (JCPDS No. 06-0249). There are no other impurity peaks, which indicate that a high purity BiOCl was prepared, and the sharp diffraction peaks suggested that BiOCl possessed good crystallinity. As shown in the diffraction data of $Bi_2O_2CO_3$, the main diffraction peaks (marked with the symbol of *) at 2θ value of 23.89°, 30.25°, 32.72°, 42.30°, 46.97°, 56.89° belong to the (011), (013), (110), (114), (020), (123) crystal planes of the tetragonal $Bi_2O_2CO_3$ (JCPDS No. 41-1488), respectively. Furthermore, for the as-synthesized Bi/BiOCl/$Bi_2O_2CO_3$, the XRD data exhibited composite characteristics after the addition of $NiCl_2$ and DMF. The intensities of the

(011), (013), (114), (116) and (123) faces of $Bi_2O_2CO_3$ were significantly decreased. Similarly, the intensities of (001), (002), (101), (102), (112) faces of BiOCl were greatly decreased. However, since BiOCl and $Bi_2O_2CO_3$ had the same structure and partially similar diffraction peaks [27], some of the diffraction peaks overlapped each other. It is noteworthy that some characteristic peaks of Bi (JPCDS No. 44-1246) also appeared in the XRD diffraction pattern, indicating the successful doping of Bi in the composite. However, due to the low content or high dispersion of metallic Bi that these diffraction peaks of Bi illustrated low intensity [40]. Lattice distortion was inevitable during the material compounding process, which resulted in a certain degree of reduction in crystallinity and lower peak intensities or wider peak widths in the diffraction patterns compared to the pure material [39]. On the other hand, it also meant that there was an interaction between BiOCl and $Bi_2O_2CO_3$ to some extent. In summary, based on the XRD diffraction pattern, Bi/BiOCl/$Bi_2O_2CO_3$ was successfully prepared.

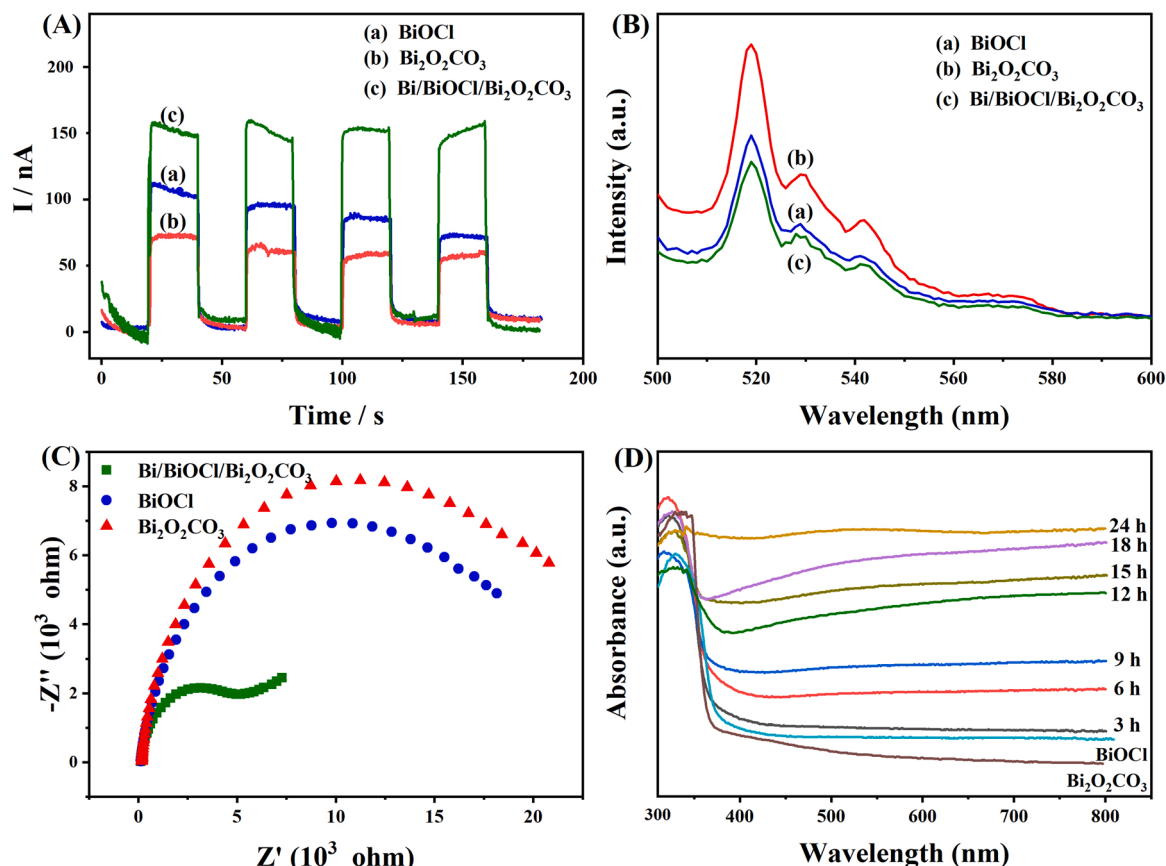To understand the function of $NiCl_2$ in the reaction system, a control

Fig. 4. Photocurrent response (A), PL spectra under 380 nm excitation (B), EIS Nyquist plot (C), and UV-Vis diffused reflectance spectra of BiOCl (a), $Bi_2O_2CO_3$ (b), $Bi/BiOCl/Bi_2O_2CO_3$ (c). (D) UV–vis diffuse reflection spectra of different nanomaterials. The dash-time presented $Bi/BiOCl/Bi_2O_2CO_3$ samples prepared with different time.

experiment was performed, where $NiCl_2$ was replaced by KCl. As seen in Fig. 2B, under the same reaction time (12 h), the XRD pattern indicated that the product should be $Bi_2O_2CO_3$, and Bi nanoparticles was not prepared. However, when KCl was replaced by $NiCl_2$, $Bi/BiOCl/Bi_2O_2CO_3$ was successfully synthesized. Based on the results, we think that $NiCl_2$ might be a catalyst to improve the reduction of Bi^{3+} by DMF. Meantime, $NiCl_2$ also provides Cl^- to form BiOCl. To prove that $NiCl_2$ only acts as catalyst and Cl- source, and Ni^{2+} does not involve the reaction, XPS was also carried out. As illustrated in Fig. 3F, no nickel element was detected in the XPS spectrum, suggesting that Ni^{2+} did not participate in the reaction, and only acts as a catalyst.

To further investigate the function of $NiCl_2$ in the preparation of $Bi/BiOCl/Bi_2O_2CO_3$, the reaction time was extended to 24 h in the presence of KCl. As illustrated in Fig. 2B, the XRD indicated that only $Bi/Bi_2O_2CO_3$ was prepared. Surprisingly, in the presence of $NiCl_2$ for 24 h, the peaks of $Bi_2O_2CO_3$ nearly disappeared and the Bi monomer became prominent extremely, which significantly demonstrated the catalysis function of $NiCl_2$ in the reaction process.

To further elucidate the composition and surface electron states, XPS was performed. As shown in Fig. 3A, the presence of Bi, O, C and Cl elements in $Bi/BiOCl/Bi_2O_2CO_3$ was confirmed by the survey of XPS. The binding energy spectra for different elements were also investigated. Fig. 3B illustrated the high-resolution spectrum of Bi 4 f, which presented two strong peaks at 158.7 and 163.9 eV, belonging to Bi $4f_{7/2}$ and Bi $4f_{5/2}$ [41], respectively. These two peaks powerful demonstrated the presence of Bi^{3+}. Meanwhile, two weak peaks were obtained at 157.1 and 162.5 eV, which were attributed to the metal monomer Bi [42]. The C 1s spectrum was shown in Fig. 3C. The peaks fixed at 284.1 and 288.2 eV were assigned to standard reference carbon and carbonate ion, respectively [28]. The binding energy spectra for Cl 2p was shown

in Fig. 3D, which was resolved into two peaks at 197.4 and 199.0 eV, attributing to Cl $2p_{3/2}$ and Cl $2p_{1/2}$ in BiOCl, respectively [39]. As recorded in Fig. 3E, the O 1s spectrum fitted to three peaks located at 530.4, 531.3, and 532.0 eV. The peak at 530.4 and 531.3 eV corresponded to Bi-O bonds in $[Bi_2O_2]^{2+}$ layer and the O atom in carbonate. The peak located at 532.0 eV resulted from the adsorbed H_2O (or surface hydroxyl groups) on the surface [39]. As illustrated in Fig. 3F, nickel element was not detected in the XPS spectrum, suggesting that Ni^{2+} did not participate in the reaction, and only acts as catalysts. To further investigate the trace of the nickel element, ICP-AES was employed to detect the content of Ni element in the filtrate after hydrothermal reaction. The result indicated that the content of Ni element in the filtrate was consistent to the content of the added $NiCl_2$. In addition, another experiment was carried out to investigate the content of Ni element in the prepared sample. Firstly, $Bi/BiOCl/Bi_2O_2CO_3$ sample was treated with 1 M HNO_3 to dissolve the nickel element. Secondly, the dispersion was filtrated and the supernatant was collected, which was further detected by ICP-AES for nickel element content. No nickel element was detected. Based on the results obtained from ICP-AES, it was further confirmed that nickel element was existed in the filtrate, not in the prepared sample.

The nitrogen adsorption-desorption isotherm was employed to describe the surface area of the synthesized samples. The specific surface areas for BiOCl and $Bi_2O_2CO_3$ showed were 1.78 and 1.73 m^2/g, respectively. Impressively, for $Bi/BiOCl/Bi_2O_2CO_3$, the specific surface area was increased greatly to 12.3 m^2/g. The large surface area can provide more reactive sites accompanying high adsorption capacity, greatly improving photocatalytic activity [43,44].
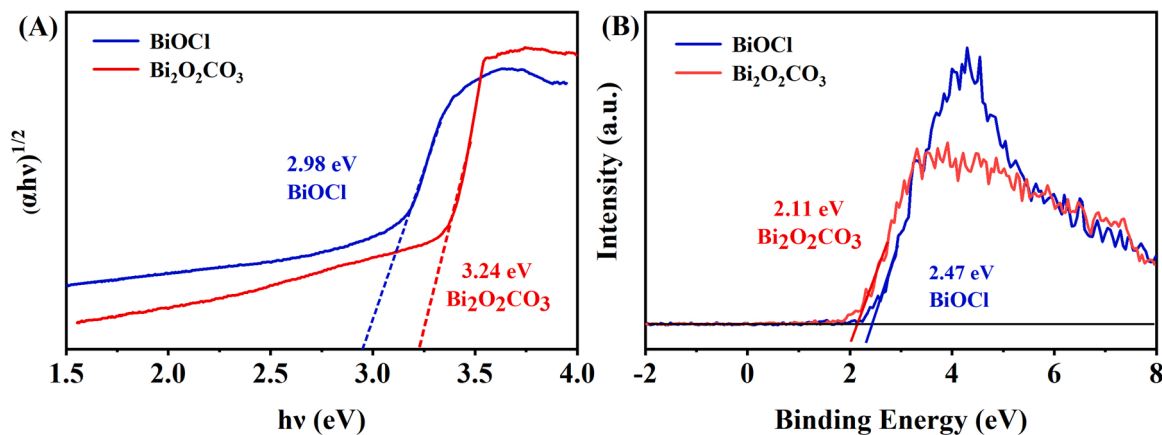
Fig. 5. (A) Tauc plots for the band gap energies originated from UV-Vis DRS. (B) VB-XPS plots.

3.2. Optical properties characterization

To investigate the migration and separation of photogenerated electron-hole pairs, the photocurrent of different samples was measured. As displayed in Fig. 4A, the photocurrent of Bi/BiOCl/Bi$_2$O$_2$CO$_3$ was greatly higher than that of BiOCl and Bi$_2$O$_2$CO$_3$, indicating the improved migration and the separation efficiency of photogenerated electron-hole pairs of Bi/BiOCl/Bi$_2$O$_2$CO$_3$.

Photoluminescence (PL) spectroscopy was further used to analyze and verify the charge separation and migration efficiency of the samples. Fig. 4B presented the PL spectra of BiOCl, Bi$_2$O$_2$CO$_3$ and Bi/BiOCl/Bi$_2$O$_2$CO$_3$ under 380 nm excitation wavelength. Compared with BiOCl and Bi$_2$O$_2$CO$_3$, the emission peak intensity of Bi/BiOCl/Bi$_2$O$_2$CO$_3$

reduced greatly, indicating the low recombination rate of photo-generated electron-hole pairs, and improved electron transfer efficiency [45].

To further investigate the electron transfer property of the samples, EIS was performed. As illustrated in Fig. 4C, the semi-circle of Bi/BiOCl/Bi$_2$O$_2$CO$_3$ in high frequency was greatly lower than that of BiOCl and Bi$_2$O$_2$CO$_3$, indicating small interface electron transfer resistance of Bi/BiOCl/Bi$_2$O$_2$CO$_3$. It can be ascribed to the doping of Bi, which facilitated the transfer of electron [46].

The optical properties of the prepared samples were also characterized by UV-Vis diffused reflectance spectroscopy. As shown in Fig. 4D, the optical adsorption edge for Bi/BiOCl/Bi$_2$O$_2$CO$_3$ was about 480 nm. It clearly suggested that the optical adsorption ability of Bi/BiOCl/
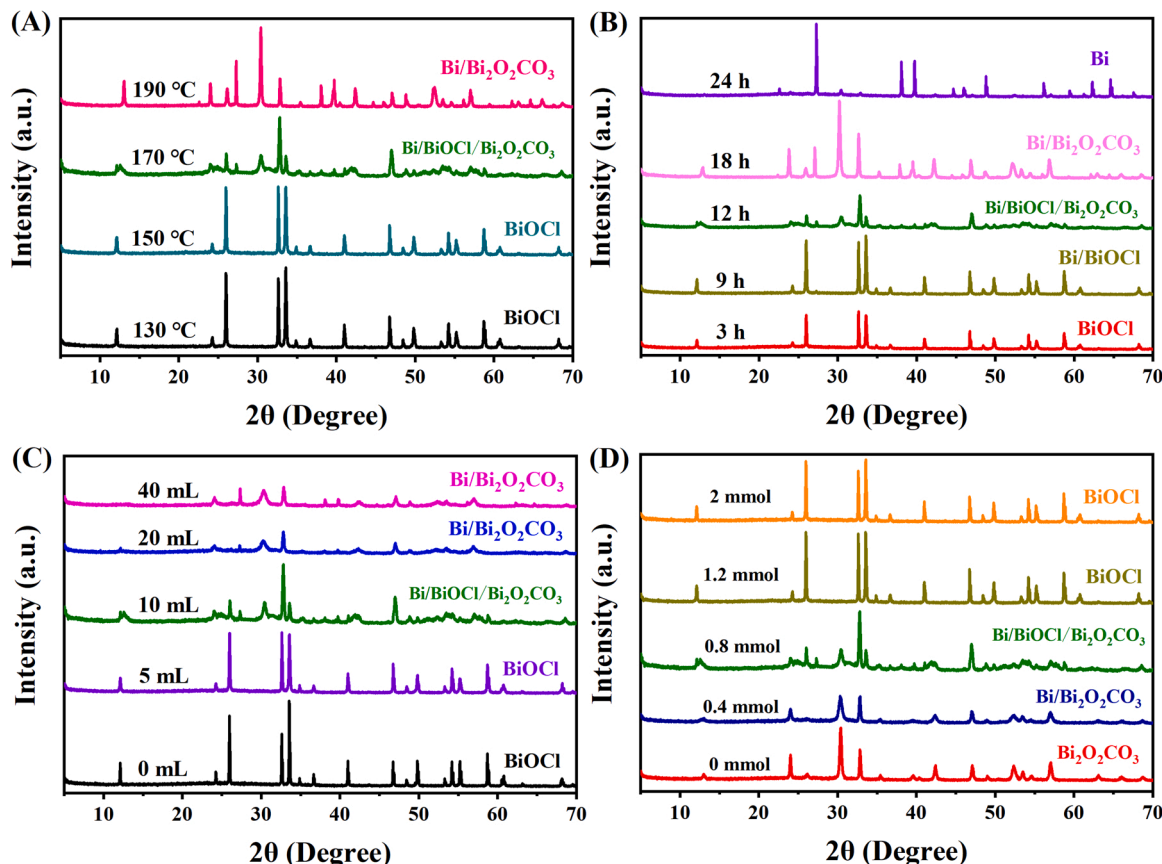

Fig. 6. XRD spectra of the samples prepared with different conditions. (A) Temperature (A), (B) reaction time, (C) DMF volume, and (D) NiCl$_2$ mass.
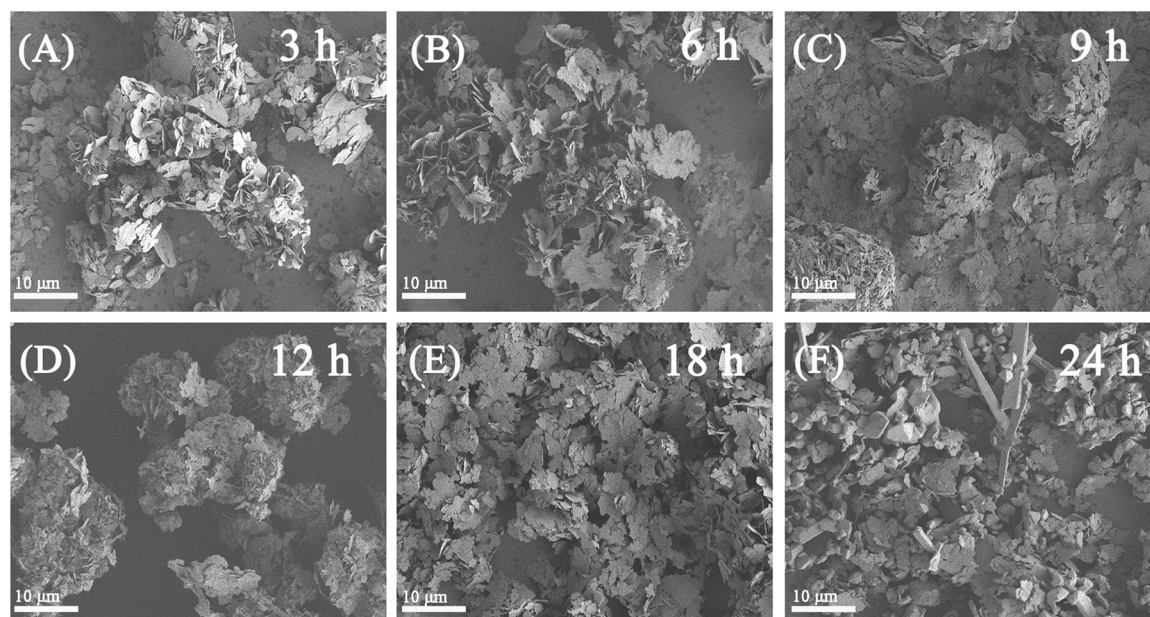
Fig. 7. SEM images of the samples prepared with different reaction time. (A) BiOCl, (B) BiOCl, (C) Bi/BiOCl, (D) Bi/BiOCl/Bi$_2$O$_2$CO$_3$, (E) Bi/Bi$_2$O$_2$CO$_3$, (F) Bi.

Bi$_2$O$_2$CO$_3$ was improved significantly [47]. The shift of Bi/BiOCl/-Bi$_2$O$_2$CO$_3$ demonstrated the efficiency of visible light activity.

3.3. Band structure determination

The light absorption properties of semiconductors are closely related to their energy band structure, and UV-Vis diffuse reflectance and Mott Schottky are used to determine the band gap structure of the samples. For semiconductors, near the edge of the optical absorption band, the following formula can be used to calculate the band gap: $(\alpha h\nu)^{1/n} = A (h\nu - E_g)$, where h, ν, α, E_g and A are Planck constant, light frequency, absorption coefficient, band gap and proportionality constant [48]. For
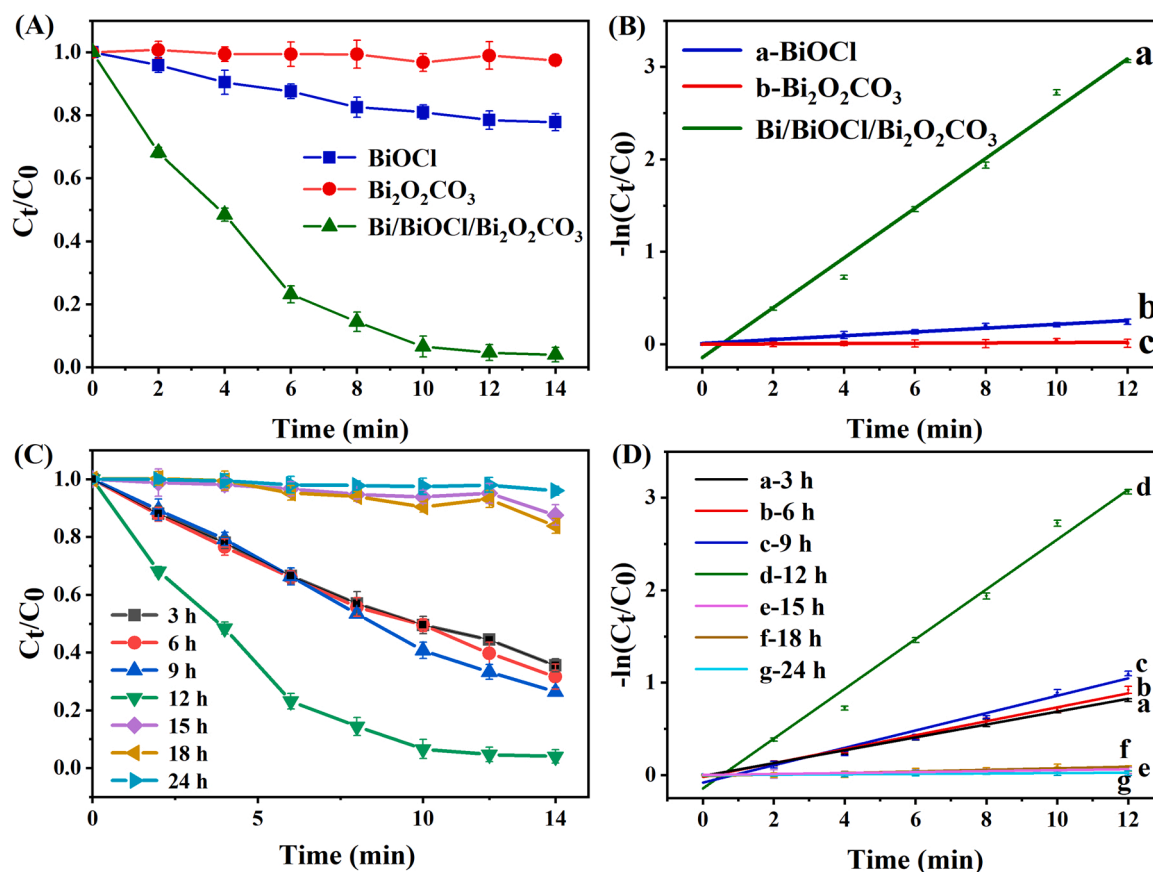

Fig. 8. (A) Photoactivity of the samples for RhB degradation under visible light. (C) Photoactivity of the samples prepared with different hydrothermal time for RhB degradation. (B, D) Plots of the relationship between $-\ln(C_t/C_0)$ and time for investigating the pseudo-first-order kinetics of RhB degradation.
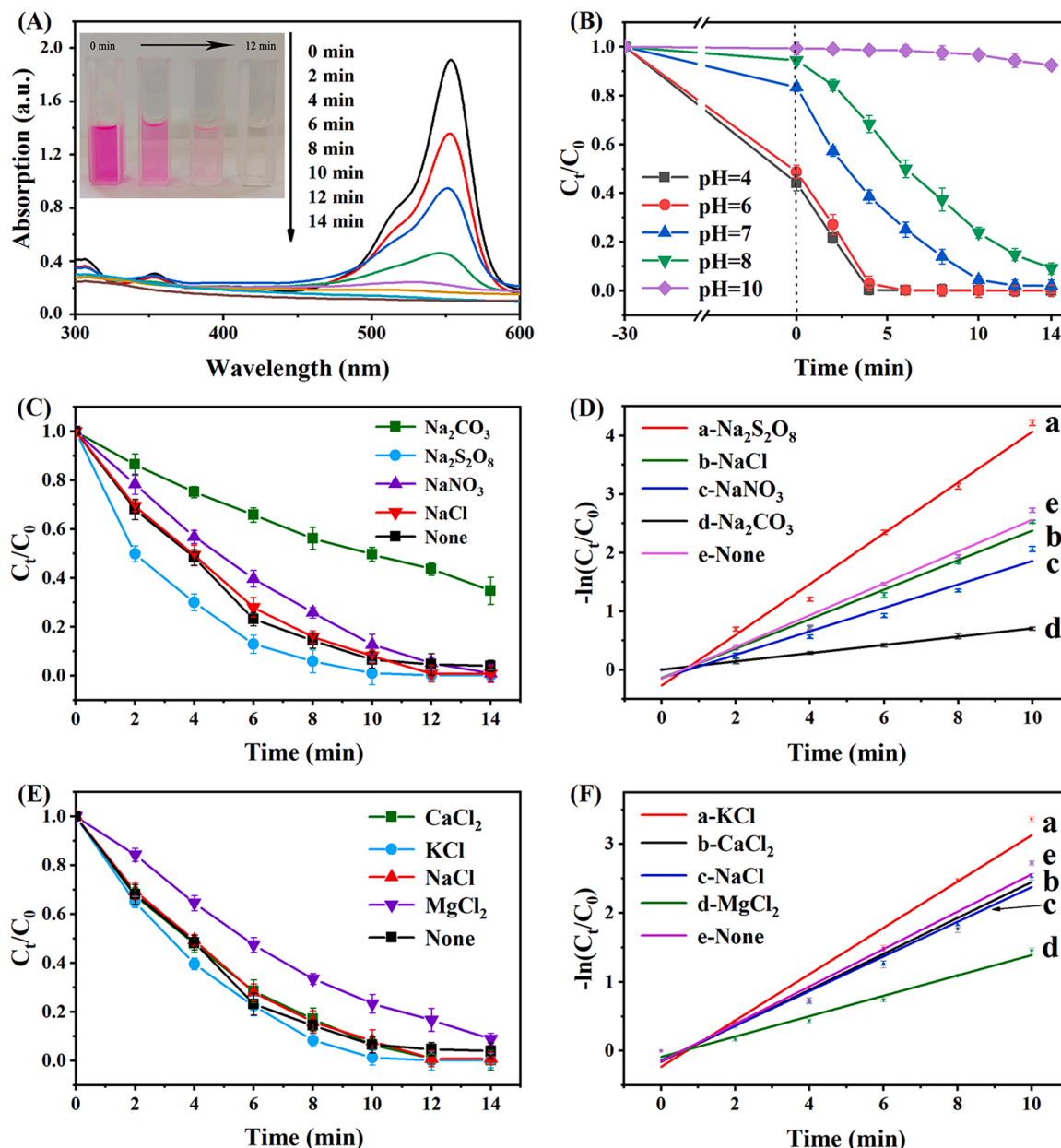
Fig. 9. (A) The adsorption spectra of RhB in the presence of Bi/BiOCl/Bi$_2$O$_2$CO$_3$ under visible light irradiation of different time. The influence of pH (B), different effects for photocatalytic degradation RhB of solution pH (B), anion (C) and cation (E) on the photodegradation efficiency of RhB. (D) and (F) were the corresponding pseudo-first-order kinetics curves. RhB concentration was 20 ppm. Anion and cation concentrations were 10 mM.

n, indirect bandgap semiconductors and direct bandgap semiconductors are taken as 2 and 1/2 separately. In this work, pure BiOCl and Bi$_2$O$_2$CO$_3$ are indirect band gap semiconductors, and hence *n* takes the value of 2.

As seen in Fig. 5A, the estimated E_g was 2.98 eV for BiOCl and 3.24 eV for Bi$_2$O$_2$CO$_3$. In addition, Fig. 5B showed the VB-XPS curves of BiOCl and Bi$_2$O$_2$CO$_3$. And the VB maximum of BiOCl and Bi$_2$O$_2$CO$_3$ were estimated to be 2.47 and 2.11 eV. According to the VB position and E_g, the CB values of BiOCl and Bi$_2$O$_2$CO$_3$ were calculated to be −0.51 and −1.13 eV, respectively.

3.4. Investigation of the formation process of Bi/BiOCl/Bi$_2$O$_2$CO$_3$

The possible growth mechanism of Bi/BiOCl/Bi$_2$O$_2$CO$_3$ heterojunction with one-step synthesis was studied under different parameters. Fig. 6A showed the XRD patterns of the samples prepared with different incubation temperature for 12 h. At relatively low temperature (130 °C,

150 °C), the diffraction peaks were indexed to the tetragonal BiOCl (JCPDS No. 06-0249). When the incubation temperature extended to 170 °C, Bi/BiOCl/Bi$_2$O$_2$CO$_3$ heterojunction was obtained. With further increasing the temperature, the peaks of BiOCl disappeared, meaning the formation of Bi/Bi$_2$O$_2$CO$_3$.

In Fig. 6B, at the initial stage of the hydrothermal process (3 h), the diffraction peaks of the samples were absolutely indexed to BiOCl. When the incubation time extended to 9 h, a weak peak at 27.165 (ascribed to the (012) plane of Bi, JPCDS No. 44-1246) appeared. After 12 h, the characteristic diffraction peaks for Bi, BiOCl and Bi$_2$O$_2$CO$_3$ were all observed. With further prolonging the incubation time, the peaks of BiOCl disappeared, and the diffraction peaks for Bi and Bi$_2$O$_2$CO$_3$ increased gradually. Finally, the sample was almost converted to Bi metal after 24 h incubation. The content of BiOCl, Bi$_2$O$_2$CO$_3$ and Bi can be controlled by varying the incubation time.
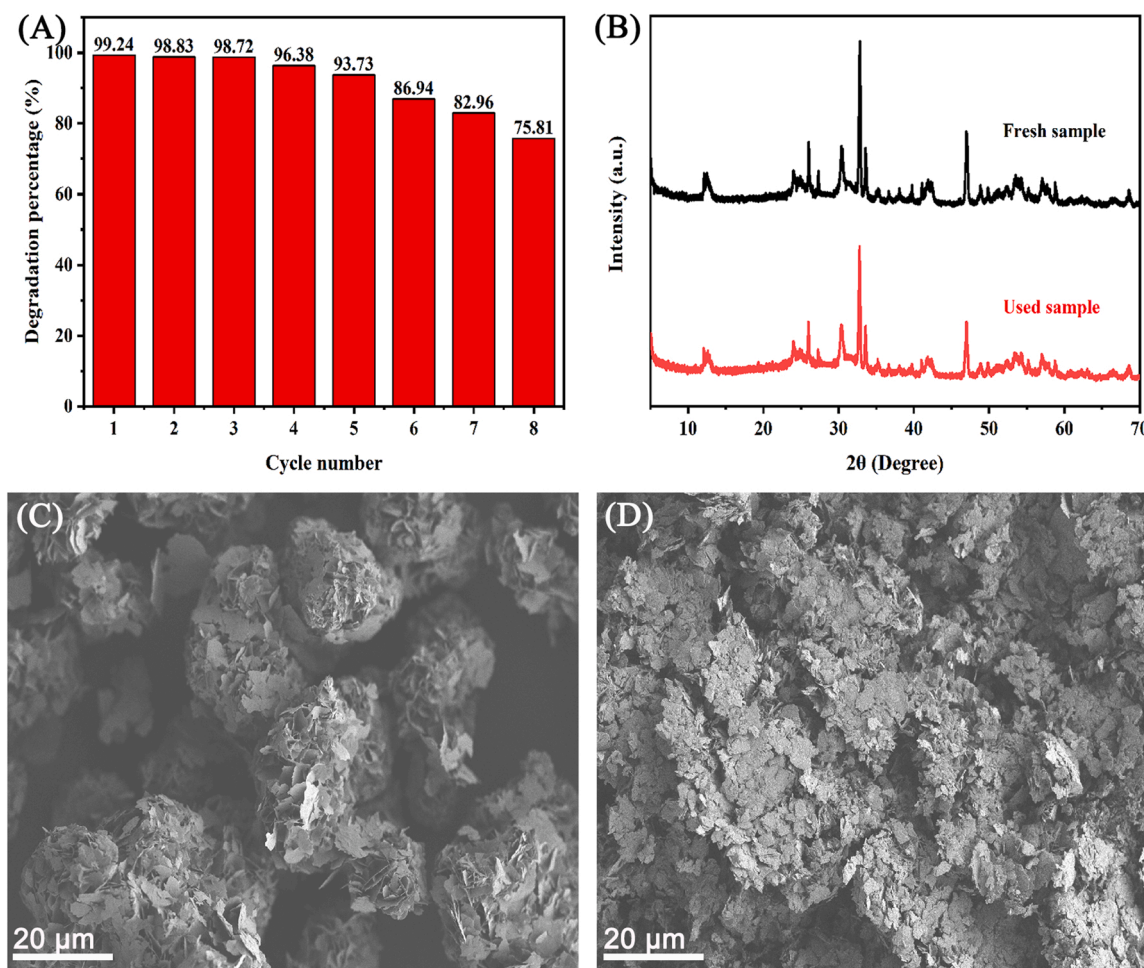
In Fig. 6C, as the volume of DMF increased to 10 mL, the product

Fig. 10. (A) Cycling runs for photocatalytic degradation of RhB in the presence of Bi/BiOCl/Bi$_2$O$_2$CO$_3$. (B) XRD pattern of Bi/BiOCl/Bi$_2$O$_2$CO$_3$ before and after eight photocatalytic reaction cycles. (C) SEM of Bi/BiOCl/Bi$_2$O$_2$CO$_3$ before degradation. (D) SEM of Bi/BiOCl/Bi$_2$O$_2$CO$_3$ after eight photocatalytic reaction cycles.

changed from BiOCl to Bi/BiOCl/Bi$_2$O$_2$CO$_3$. However, the product was changed to be Bi/Bi$_2$O$_2$CO$_3$ when the DMF volume was increased to 20 and 40 mL. It indicated that too much DMF would inhibit the formation of BiOCl and too little would not be sufficient to form Bi and Bi$_2$O$_2$CO$_3$. Meanwhile, as shown in Fig. 6D, the excess NiCl$_2$ provided a sufficient source of Cl, leading to a large production of BiOCl. Minimal amounts of NiCl$_2$ were weak in catalysis of Bi reduction reaction and did not provide an enough source of Cl to support the growth of BiOCl. In summary, ternary heterojunctions could be ensured by adjusting the amount of DMF and NiCl$_2$ reasonably and controlling the reaction time and temperature.

The formation process for Bi/BiOCl/Bi$_2$O$_2$CO$_3$ heterojunction was also investigated by SEM. As can be seen in Fig. 7A-D, with increasing the incubation time, the sample structure changed from irregular nanosheets to the regular microspheres with sizes of about 15 μm comprising numerous nanosheets. When the incubation time exceeded 12 h, as seen in Fig. 7E, the microspheres became loose and some of them collapsed. Then, with further increasing incubation time, these microspheres shattered (Fig. 7F), and some stacked nanosheet structures were observed. Finally, the block construction was obtained with the formation of Bi-metal.

3.5. Photocatalytic activity

The photocatalytic activity of the as-prepared Bi/BiOCl/Bi$_2$O$_2$CO$_3$ photocatalyst was evaluated by the removal of RhB as a function of time under visible light irradiation. As shown in Fig. 8A, for Bi/BiOCl/

Bi$_2$O$_2$CO$_3$, more than 99.0% of RhB was degraded after 12 min of irradiation, while only 21.5% and 2.25% of RhB was degraded under the same photocatalytic conditions by BiOCl and Bi$_2$O$_2$CO$_3$, respectively. These results clearly demonstrated the higher photocatalytic activity of Bi/BiOCl/Bi$_2$O$_2$CO$_3$ comparing with pure BiOCl and Bi$_2$O$_2$CO$_3$.

The kinetic of pollutant degradation was simulated using the quasi-first-order model with the equation of $-\ln(C_t/C_0) = k_{ap}t$ [49], where C_t was the concentration of pollutants after degradation of t minutes, C_0 was the initial concentration of pollutants, t was the degradation time and k_{ap} was the reaction rate constant. The reaction constant (min^{-1}) for BiOCl, Bi$_2$O$_2$CO$_3$ and Bi/BiOCl/Bi$_2$O$_2$CO$_3$ were 0.02066, 0.0016, 0.2694, respectively (Fig. 8B). The reaction rate constants for Bi/BiOCl/Bi$_2$O$_2$CO$_3$ were 12.58 and 168.38 times higher than those for BiOCl and Bi$_2$O$_2$CO$_3$, respectively. These results further proved the improved photocatalytic activity of Bi/BiOCl/Bi$_2$O$_2$CO$_3$.

The effect of the hydrothermal time of the photoactivity of the samples was also evaluated. As shown in Fig. 8C, the hydrothermal time greatly influence the photoactivity of the prepared samples. Based on the investigation by XRD (Fig. 6), the composition of the complex was depended on the hydrothermal time. Combining these two results, it can be seen that the composition of the composite has a great influence on the photocatalytic activity. With increasing the hydrothermal time from 3 to 12 h, the photoactivity increased gradually. However, with furthering increasing hydrothermal time, the photoactivity decreased significantly. According to the XRD results, the samples was BiOCl with the time of 3 and 6 h, Bi/BiOCl for 9 h, Bi/BiOCl/Bi$_2$O$_2$CO$_3$ for 12 h, Bi/Bi$_2$O$_2$CO$_3$ for 15 and 18 h, and mainly Bi for 24 h. Therefore, the
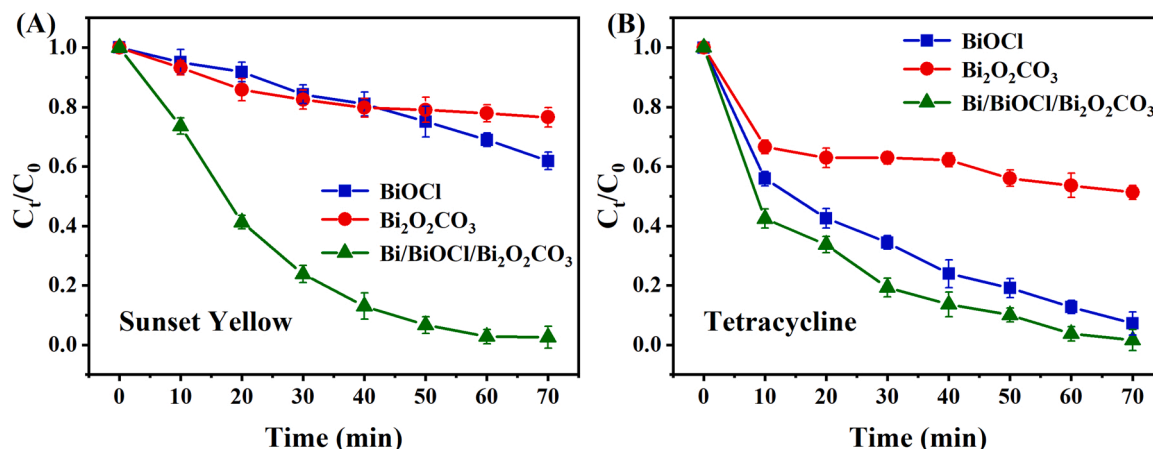
Fig. 11. Photocatalytic degradation activity of different photocatalysts towards sunset yellow (A) and tetracycline (B) under visible light irradiation.

photoactivity of Bi/BiOCl/Bi$_2$O$_2$CO$_3$ was greatly higher than that of Bi/BiOCl, Bi/Bi$_2$O$_2$CO$_3$, and Bi. Of course, the k_{ap} of Bi/BiOCl/Bi$_2$O$_2$CO$_3$ was greatly higher than other samples with different preparation time.

As shown in Fig. 9A, the maximum adsorption peak of RhB decreased with extending the time under visible-light irradiation in 1 mg/mL dispersion of Bi/BiOCl/Bi$_2$O$_2$CO$_3$. It is remarkable that the maximum absorption peak on the spectrum nearly disappeared after 10 min. The color changes of RhB were illustrated in the inset of Fig. 9A. During the photocatalytic degradation process, no shift at the maximum absorption peak was observed, indicating that no other colored derivatives were produced in the intermediate process [40]. However, the actual system of environmental pollutants is inevitable under different pH and various co-existed inorganic ions. As shown in Fig. 9B, the effect of pH for photodegradation efficiency of Bi/BiOCl/Bi$_2$O$_2$CO$_3$ was investigated. When pH was tuned from the initial pH 7 to pH 4 and pH 6, the adsorption properties of the catalyst were greatly enhanced, with approximately 50% of RhB adsorbed, followed by completed degradation of RhB after 5 min under visible light, indicating that the addition of H$^+$ facilitated the adsorptive synergistic degradation properties of materials. In contrast, the catalyst's performance was reduced to a certain extent when the pH was set to 8, with only 85.1% of the dye was degraded after 12 min under visible light irradiation. At pH= 10, the degradation of the material was totally inhibited, with only 7.6% degraded after the same time under light exposure. These results have demonstrated that the degradation performance of Bi/BiOCl/Bi$_2$O$_2$CO$_3$ under weak acidic as well as neutral conditions was favorable.

In view of the practical applications of photocatalysis, the photocatalyst is inevitably used in complicated environment containing various anions and cation. The coexisted inorganic ions are an important factor to influence the photocatalytic activity of catalyst [50–52]. Therefore, the effect of some anions nad cations on the photocatalytic activity of Bi/BiOCl/Bi$_2$O$_2$CO$_3$ towards RhB was investigated, where the concentration of ions were 10 mM according to previous work as descried in Supplementary Material [53–57]. As shown in Fig. 9C and D, the degradation efficiency was 99.2%, 94.8%, 99.8% and 65.2% with the addition of NaCl, Na$_2$NO$_3$, Na$_2$S$_2$O$_8$ and Na$_2$CO$_3$, respectively. Cl$^-$ almost did not affect the degradation of the system, while NO$_3^-$ had a small inhibitory effect on the degradation. However, the photocatalytic activity was facilitated to some extent by S$_2$O$_8^{2-}$, probably because of the production of strongly oxidizing SO$_4^-$·radicals during the process [58], which accelerated the degradation reaction with a reaction rate constant 1.47 times higher than that of pure Bi/BiOCl/Bi$_2$O$_2$CO$_3$. Conversely, as CO$_3^{2-}$ can trap h$^+$, the presence of CO$_3^{2-}$ in the system could lead to weaker oxidation of h$^+$ and thus affect degradation performance [59].

In Fig. 9E and F, there were no significant changes in the system when CaCl$_2$ was introduced, and a small contribution to degradation was made by the addition of KCl. The addition of Mg^{2+} hindered the

degradation process, resulting in a decrease in the degradation rate to 91.2%. according to the investigation of the influence of anion and cation on the photodegradation effiiciency of Bi/BiOCl/Bi$_2$O$_2$CO$_3$ on RhB, the sample can resist the influence of some anions and cations, presenting good anti-interference property.

3.6. Photocatalytic cycle stability and reusability

In addition to excellent photocatalytic activity, reusability and stability have significant impact on the practical industrial application of photocatalysts. Therefore, cycling photocatalytic experiments were performed to evaluate the reusability of the catalyst. As shown in Fig. 10A, after five cycles, about 93.73% of RhB was degraded, which was slightly lower than that of the first cycle (99.24%). To our surprise, the catalyst compound retained good activity after eight cycles, where about 75.81% of RhB was degraded. It has been demonstrated that Bi/BiOCl/Bi$_2$O$_2$CO$_3$ can maintain stable degradation activity during multiple photocatalytic processes. The leaching of Bi ions was investigated using ICP-AES. The result indicated that only 0.8 ng/mL Bi ions were leached into the solution after photocatalytic degradation of RhB for 30 min, indicating the strong stability of Bi element in Bi/BiOCl/Bi$_2$O$_2$CO$_3$ in solution with degradation process.

Moreover, the crystal structure of Bi/BiOCl/Bi$_2$O$_2$CO$_3$ before and after use was investigated by XRD pattern. As seen in Fig. 10B, the positions of XRD peaks stayed the same after eight cycles. However, the intensity of the XRD peaks decreased. In Fig. 10D, the morphology of Bi/BiOCl/Bi$_2$O$_2$CO$_3$ was changed after photocatalytic reaction. The spherical structure was destroyed and stacked into block or lamellar structure after crushing. Moreover, the surface became rough and the smoothness was greatly reduced. These results indicated that after a series of photocatalytic degradations the structure and crystalline shape of Bi/BiOCl/Bi$_2$O$_2$CO$_3$ changed a little. Its morphology was irreversibly damaged, which influenced the photocatalytic effect. The stability can be further confirmed by the chemical constituent after degradation analyzed by XPS. The survey spectrum and high-resolution spectra (Fig. S10) also presented a very similar result to the fresh Bi/BiOCl/Bi$_2$O$_2$CO$_3$. The results revealed the structure is stable even after cycle photocatalytic degradation processes.

3.7. Photocatalytic degradation for a wide range of applications

To evaluate the widespread applicability of the prepared Bi/BiOCl/Bi$_2$O$_2$CO$_3$ photocatalyst, the nanocomposite was employed to degrade another dye (sunset yellow) and a kind of antibiotic (tetracycline). The degradation results were also compared with BiOCl and Bi$_2$O$_2$CO$_3$. As illustrated in Fig. 11A and B, the photocatalytic activity for Bi/BiOCl/Bi$_2$O$_2$CO$_3$ was greatly higher than that of BiOCl and Bi$_2$O$_2$CO$_3$. From the

Table 1
The kinetic parameter of reaction rate constant for different pollutants.

Sample	Reaction rate constant (min^{-1})		
	RhB	Sunset yellow	Tetracycline
BiOCl	0.0207	0.0058	0.0359
$Bi_2O_2CO_3$	0.0016	0.0050	0.0114
$Bi/BiOCl/Bi_2O_2CO_3$	0.2694	0.0545	0.0542

corresponding kinetic parameters in Table 1, the construction of

heterojunction enabled $Bi/BiOCl/Bi_2O_2CO_3$ photocatalyst to effectively degrade different kinds of pollutants, and improved the degradation rate to a certain extent.

3.8. Mineralization activity

To further evaluate the photocatalytic activity of $Bi/BiOCl/Bi_2O_2CO_3$, the mineralization degree (illustrated by TOC content) of the three organic pollutants was investigated under visible light. To perform it, the organic pollutants (20 ppm) were degraded by 1 mg/mL Bi/
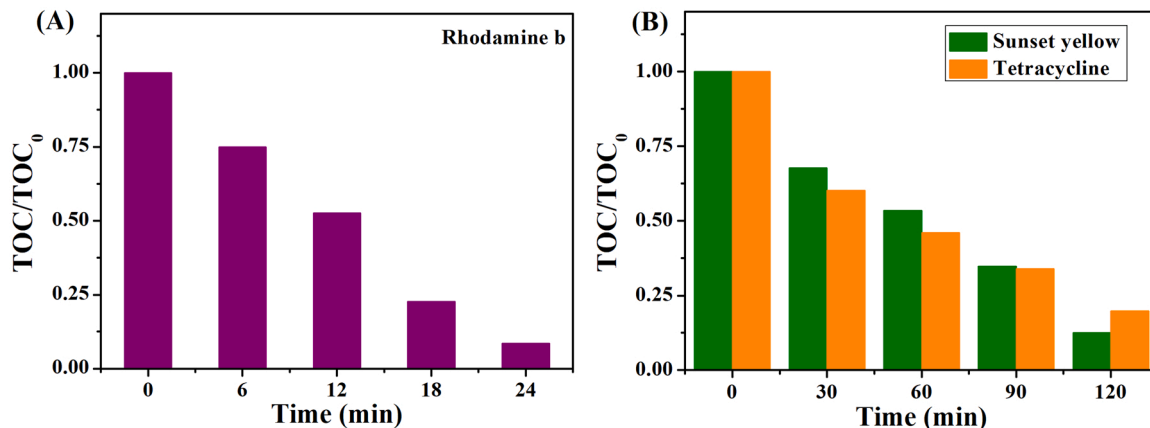

Fig. 12. The removal rate of TOC in RhB (A) and sunset yellow and tetracycline (B). The concentrations for pollutants were 20 ppm.
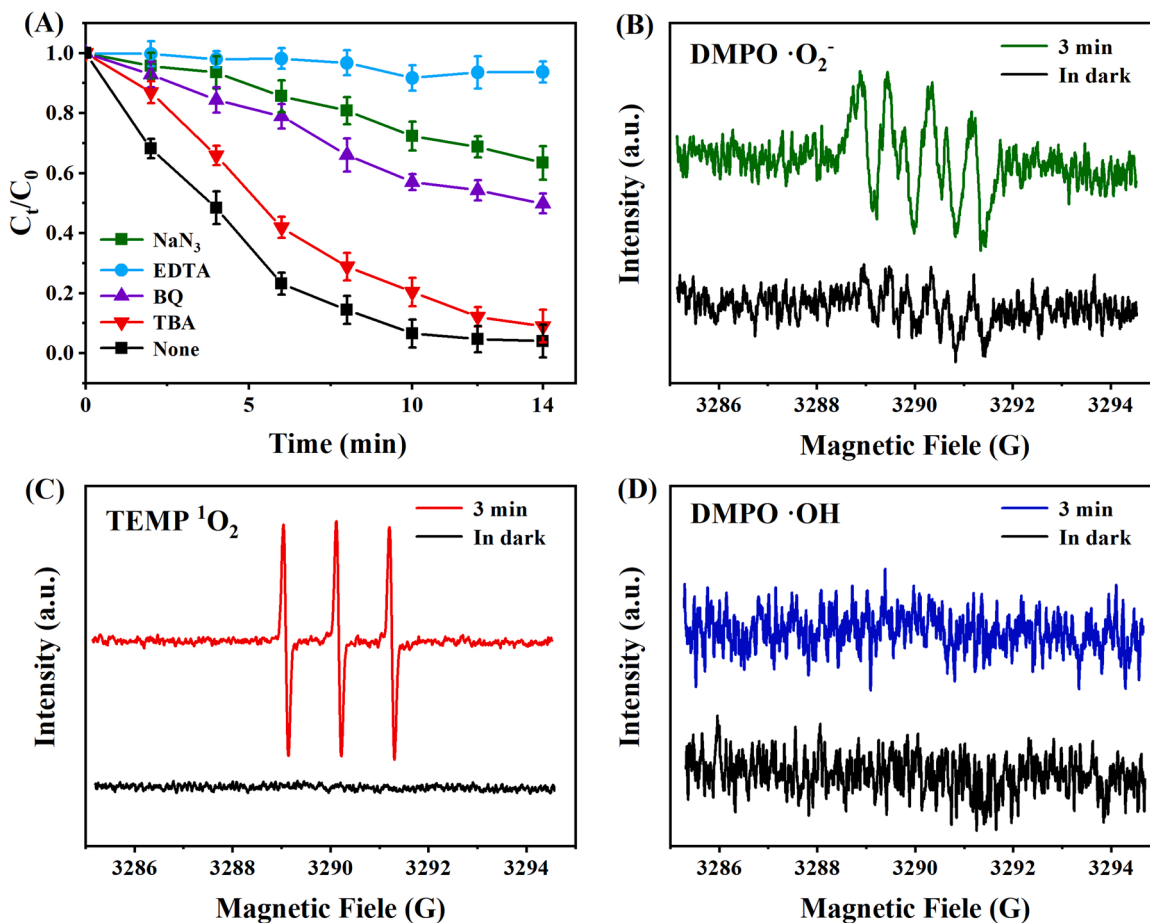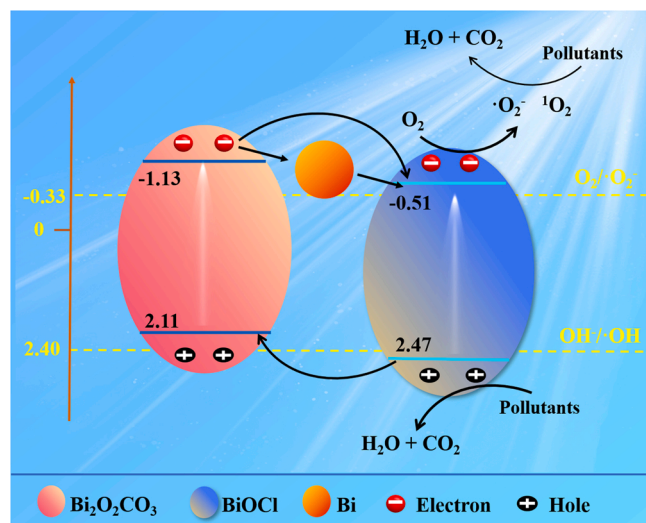

Fig. 13. (A) Active species trapping experiments of $Bi/BiOCl/Bi_2O_2CO_3$ for degrading RhB. ESR signals of the DMPO-·O_2^- (B), TEMP-$^1O_2$ (C) and DMPO-·OH (D) under visible-light irradiation for 3 min.

Scheme 1. Schematic diagram of the photocatalytic mechanism and charge transfer in the heterojunction.

BiOCl/Bi$_2$O$_2$CO$_3$ under visible light irradiation. As illustrated in Fig. 12, with extending the degradation time, the TOC content decreased gradually for the three organic pollutants. Bi/BiOCl/Bi$_2$O$_2$CO$_3$ presented different removal rate for the three pollutants, which might be ascribed to the different molecule structure. The maximum TOC removal rate for RhB, sunset yellow and tetracycline were about 91.46%, 87.53% and 80.13%, respectively. The TOC removal rate for RhB was compared with some of previous work and the results were listed in Table S1. These results demonstrated that the photocatalytic degradation of the three pollutants under visible light irradiation was accompanied by partial mineralization.

3.9. Analysis of active species

To demonstrate the types of free radicals produced during photocatalysis and to elucidate the mechanism of radical action, radicals trapping experiments have been carried out. Benzoquinone (BQ), sodium azide (NaN$_3$), tert-butanol (TBA) and disodium ethylenediamine tetraacetate (EDTA) were used as scavengers for·O$_2^-$, ^{1}O$_2$,·OH and hole (h$^+$) [60,61], respectively. The photocatalytic degradation effect of Bi/BiOCl/Bi$_2$O$_2$CO$_3$ for RhB under the different circumstances was shown in Fig. 13A. The decomposition rate of RhB was slightly reduced by the addition of TBA to the catalytic system, which indicated that·OH did not play a crucial role in the photocatalytic degradation process. When EDTA was added, there was a significant decrease in the degradation rate of RhB, suggesting that h$^+$ worked importantly in the overall photocatalytic process. Likewise, the addition of BQ and NaN$_3$ inhibited the decomposition of RhB, respectively. Based on these preliminary free radicals scavenging experiments, it was shown that the RhB degradation process was dominated by h$^+$, ^{1}O$_2$ and·O$_2^-$.

The electron spin resonance (ESR) technique was also employed to detect the active free radicals in the photocatalytic process, where DMPO and TEMP were used as trapping reagents for radicals (·O$_2^-$ and·OH) and ^{1}O$_2$, respectively. The results were shown in Fig. 13B–D. After three minutes of visible light, ESR signal peaks of ^{1}O$_2$ and·O$_2^-$ were observed, indicating the compound materials could produce a large amount of ^{1}O$_2$ and·O$_2^-$ under sunlight irradiation. This is consistent with the results of free radical scavenging experiments and further confirms the important role of ^{1}O$_2$ and·O$_2^-$ in degradation. However, though TBA inhibition experiment indicated·OH played very weak effect in photocatalytic process, no characteristic signals were observed for·OH (Fig. 13D) indicating the generation of·OH radicals were not achieved for Bi/BiOCl/Bi$_2$O$_2$CO$_3$. The similar phenomena were also reported for

Bi$_2$O$_2$CO$_3$/BiOCl [28,39] and Bi$_2$O$_2$CO$_3$/BiOBr [62]. Combining the results obtained by radicals trapping experiments and ESR, it can confirm that h$^+$, ^{1}O$_2$ and·O$_2^-$ play important functions in the photocatalytic process.

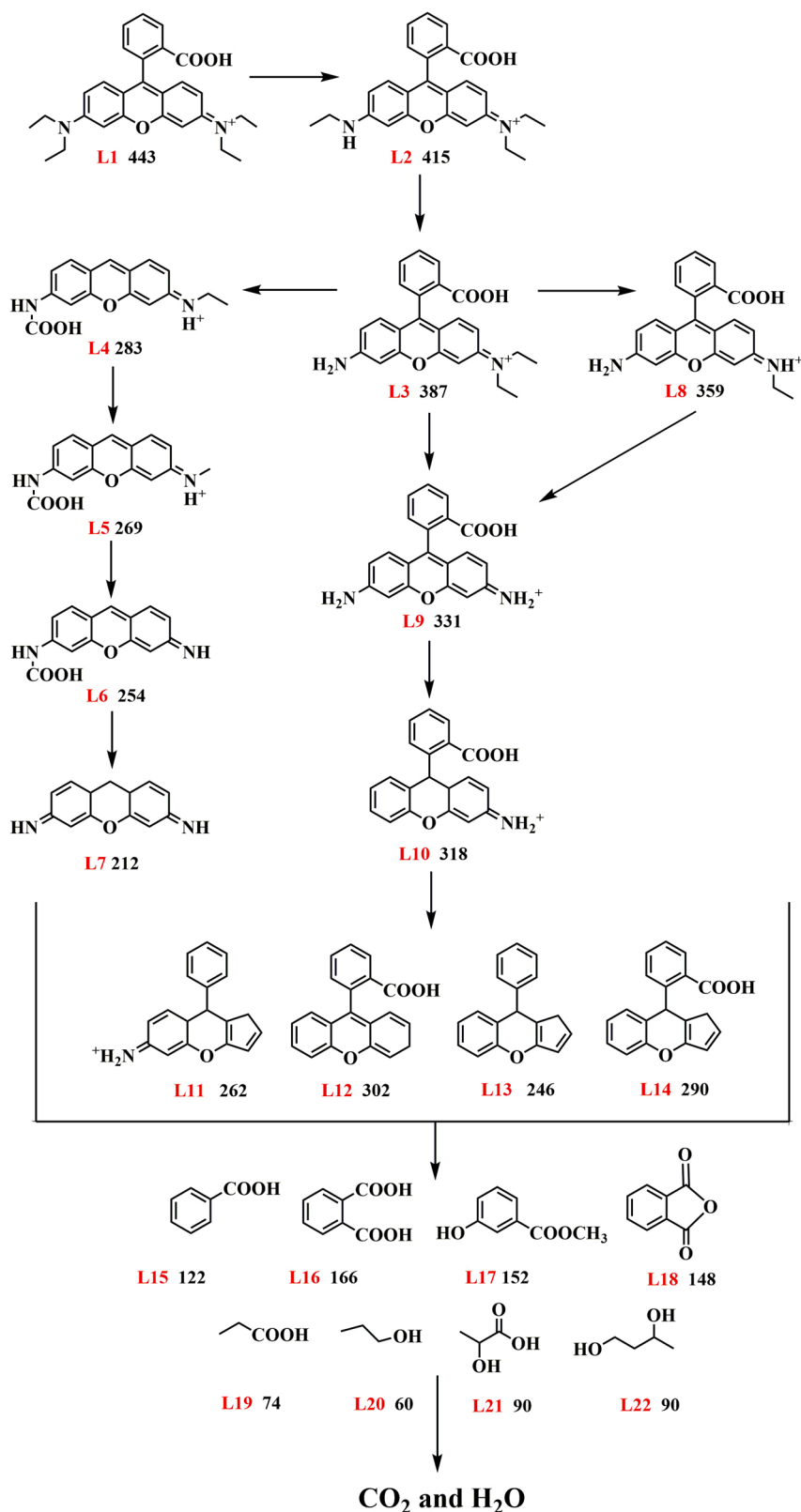### 3.10. Photocatalytic degradation mechanism

Up to now, we have discussed the outstanding photocatalytic properties and energy band structure of Bi/BiOCl/Bi$_2$O$_2$CO$_3$ in detail, as well as the functions of reactive radicals during the photocatalytic process. Based on the above results, we have proposed the corresponding RhB degradation mechanism and the energy bandgap structure, as shown in Scheme 1. Under the simulated light excitation, the electrons in BiOCl and Bi$_2$O$_2$CO$_3$ are photoexcited to their CB, with the holes remaining in VB. The plasmonic Bi can transform the photons energy into a partial electromagnetic field, which remarkably accelerates the separation of photogenerated electron-hole pairs. Electrons in the CB of Bi$_2$O$_2$CO$_3$ are rapidly transferred to the CB of BiOCl. The CB potential of BiOCl is −0.51 eV, which is more negative than that of the O$_2$/·O$_2^-$ redox potential (−0.33 eV) [63], could reduce the O$_2$. On the other hand, photogenerated holes accumulate on the VB of Bi$_2$O$_2$CO$_3$. The VB potential of Bi$_2$O$_2$CO$_3$ is 2.11 eV, which is negative than that of the OH$^-$/·OH potential (2.40 eV) [64]. So, the VB of Bi$_2$O$_2$CO$_3$ cannot produce·OH radicals efficiently. Moreover, the VB of BiOCl is 2.47 eV, which is similar with that of the OH$^-$/·OH potential (2.40 eV), presenting weak ability to produce OH$^-$/·OH. In addition, the h$^+$ at the BiOCl can directly oxidize the pollutants.

In brief, the photogenerated carriers transfer to the catalyst surface to activate the adsorbed O$_2$ present, forming a series of reactive oxygen species (ROS) ^{1}O$_2$ and·O$_2^-$. Consequently, these ROS collaborate with h$^+$ to degrade the pollutants and ultimately mineralize them to H$_2$O and CO$_2$. The heterostructure efficiently facilitates the separation of photogenerated carriers, enabling the catalyst to rapidly generate active components for the degradation of pollutants [64].

3.11. Degradation pathways and toxicity of degradation products

The degradation pathway of RhB under visible-light irradiation using Bi/BiOCl/Bi$_2$O$_2$CO$_3$ as photocatalyst was speculated using LC-MS. The products were labeled as L1 – L22. The corresponding MS spectra were illustrated in Supplementary Materials. As shown in Scheme 2, because of nucleophilic substitution reaction with the ethyl [65], the RhB (L1, m/z 443) was attacked by e$^-$, formed into N, N, N-diethyl-N'-ethylrhodamine (L2, m/z 415). The active species such as·O$_2^-$ and h$^+$ could attack the central carbon and further degraded through de-ethylation process. Next, L2 continued to de-ethylated into N, N-diethylrhodamine (L3, m/z 387). Then, N-deethylation and carboxylation led to the formation of L4 (m/z 283), it is a typical benzene removal intermediates [66]. Intermediate L4 was further degraded to L5, L6 and L7, corresponding to m/z value of 269, 254 and 212. In another pathway, N, N'-monomethylethylrhodamine (L8, m/z 359) and N, N'-ethylrhodamine (L9, m/z 331) were caught via de-ethylate reaction of L3 [67]. The L10 (m/z 318) was the product when -NH bonds were broken. Next, L10 was degraded to several molecules, such as L11 (m/z 262), L12 (m/z 302), L13 (m/z 246), L14 (m/z 290). Furthermore, RhB was broken down into several small molecules, including benzoic acid (L15, m/z 122), phthalic acid (L16, m/z 166), propanoic acid (L19, m/z 74), 2-hydroxypropanoic acid (L21, m/z 90) [68]. The photocatalytic-process is not halted after the decomposition of the organic dye, it towards the full mineralization of the organic matter to form CO$_2$ and H$_2$O [69].

To further evaluate the toxicology of degradation products, the influence in mung bean seedlings was investigated. In this work, the mung bean seeds were incubated with sterilized water (as control), RhB solution (20 ppm) and degraded solution of RhB, respectively. As illustrated in Fig. 14, when mung bean seeds were incubated under RhB

Scheme 2. Photocatalytic degradation pathway of RhB under simulated light irradiation.

solution, the seedlings developed slowly with short plant length, especially the root is short compared with control samples. Additionally, in photocatalytic degradation solution, the development of mung bean seedlings was greatly improved. Seedlings showed little apparent difference in stem length from the control group, which should be ascribed

to the reduced toxicity of degradation products. Moreover, the root development of mung bean seedlings after incubation with degraded solution was improved compared with control and RhB solution. It might be explained as the fact that there are some nutritional contents or nutritional elements in the degraded solution, which might promote the

Fig. 14. Toxicological evaluation of degradation products.

root elongation and lateral root development of mung bean seedling.

4. Conclusions

In conclusion, an efficient and novel heterojunction photocatalyst Bi/BiOCl/Bi$_2$O$_2$CO$_3$ was first successfully prepared using DMF as the carbon source and reducing agent. Under visible light irradiation, the photocatalytic degradation efficiency of the composite catalyst for pollutants was significantly increased, with 99% of RhB was removed within 12 min. The experimental results showed that the enhanced degradation properties and improved stability were attributed to the synergistic effect of heterojunctions and Bi nanoparticles. Then, by evaluating reaction pathways and the toxicology of degradation products, we presented a possible degradation process and also demonstrated the decreased toxicity of the degradation products. The above results reflect the great potential of Bi/BiOCl/Bi$_2$O$_2$CO$_3$ for industrial applications. The preparation process of Bi/BiOCl/Bi$_2$O$_2$CO$_3$ photocatalyst was simple and rapid, it can be expected to provide a novel idea for the design of other metal nanoparticle-based heterojunction semiconductor materials.

CRediT authorship contribution statement

Lingsong Wang: Data curation, Formal analysis, Investigation, Methodology, Validation, Project administration, Writing – review & editing. **Huanshun Yin**: Data curation, Formal analysis, Funding acquisition, Project administration, Validation, Supervision, Writing – review & editing. **Suo Wang**: Data curation, Formal analysis, Investigation, Methodology. **Jun Wang**: Data curation, Project administration, Validation, Supervision, Writing – review & editing. **Shiyun Ai**: Project administration, Validation, Supervision.

Declaration of Competing Interest

The authors declare that they have no known competing financial interests or personal relationships that could have appeared to influence the work reported in this paper.

Acknowledgements

References

[1] D. Lin, M. Gao, L. You, Y. Li, Z. Li, L. Guo, T. Li, M. Liu, Fabrication of novel Ag/AgVO$_3$/WO$_3$ homojunction/heterojunction nanomaterials with highly enhanced photocatalytic activity- investigation on type l plus Z-scheme mechanism, J. Alloy. Compd. 846 (2020), 156274, https://doi.org/10.1016/j.jallcom.2020.156274.

[2] F. Chen, Y. Cao, D. Jia, Facile synthesis of Bi$_2$S$_3$ hierarchical nanostructure with enhanced photocatalytic activity, J. Colloid Interface Sci. 404 (2013) 110–116, https://doi.org/10.1016/j.jcis.2013.04.013.

[3] H. Zhang, C. Lu, H. Hou, Y. Ma, S. Yuan, Facile morphology-controlled synthesis of Co$_3$O$_4$ nanostructure on carbon cloth and their morphology-dependent pseudocapacitive performances, J. Alloy. Compd. 797 (2019) 970–977, https://doi.org/10.1016/j.jallcom.2019.05.206.

[4] M. Hou, J. Gao, L. Yang, S. Guo, T. Hu, Y. Li, Room temperature gas sensing under UV light irradiation for Ti$_3$C$_2$Tx MXene derived lamellar TiO$_2$-C/g-C$_3$N$_4$ composites, Appl. Surf. Sci. 535 (2021), 147666, https://doi.org/10.1016/j.apsusc.2020.147666.

[5] G. Huang, S. Li, S. Liu, L. Zhu, Q. Wang, Ti$_3$C$_2$ MXene-modified Bi$_2$WO$_6$ nanoplates for efficient photodegradation of volatile organic compounds, Appl. Surf. Sci. 503 (2020), 144183, https://doi.org/10.1016/j.apsusc.2019.144183.

[6] A. El Golli, M. Fendrich, N. Bazzanella, C. Dridi, A. Miotello, M. Orlandi, Wastewater remediation with ZnO photocatalysts: green synthesis and solar concentration as an economically and environmentally viable route to application, 112226-112226, J. Environ. Manag. 286 (2021), https://doi.org/10.1016/j.jenvman.2021.112226.

[7] H. Liu, Y. Ma, J. Chen, M. Wen, G. Li, T. An, Highly efficient visible-light-driven photocatalytic degradation of VOCs by CO$_2$-assisted synthesized mesoporous carbon confined mixed-phase TiO$_2$ nanocomposites derived from MOFs, Appl. Catal. B: Environ. 250 (2019) 337–346, https://doi.org/10.1016/j.apcatb.2019.03.054.

[8] W. Zhang, G. Li, H. Liu, J. Chen, S. Ma, M. Wen, J. Kong, T. An, Photocatalytic degradation mechanism of gaseous styrene over Au/TiO$_2$@CNTs: relevance of superficial state with deactivation mechanism, Appl. Catal. B: Environ. 272 (2020), 118969, https://doi.org/10.1016/j.apcatb.2020.118969.

[9] W. Zou, B. Gao, Y.S. Ok, L. Dong, Integrated adsorption and photocatalytic degradation of volatile organic compounds (VOCs) using carbon-based nanocomposites: a critical review, Chemosphere 218 (2019) 845–859, https://doi.org/10.1016/j.chemosphere.2018.11.175.

[10] K. Qi, W. Lv, I. Khan, S.-y Liu, Photocatalytic H$_2$ generation via CoP quantum-dot-modified g-C$_3$N$_4$ synthesized by electroless plating, Chin. J. Catal. 41 (2020) 114–121, https://doi.org/10.1016/S1872-2067(19)63459-5.

[11] K. Qi, S.-y Liu, A. Zada, Graphitic carbon nitride, a polymer photocatalyst, J. Taiwan Inst. Chem. Eng. 109 (2020) 111–123, https://doi.org/10.1016/j.jtice.2020.02.012.

[12] H. Zhang, Y. Li, W. Li, C. Zhuang, C. Gao, W. Jiang, W. Sun, K. Qi, Z. Sun, X. Han, Designing large-sized cocatalysts for fast charge separation towards highly efficient visible-light-driven hydrogen evolution, Int. J. Hydrog. Energy 46 (2021) 28545–28553, https://doi.org/10.1016/j.ijhydene.2021.06.134.

[13] W. Li, C. Zhuang, Y. Li, C. Gao, W. Jiang, Z. Sun, K. Qi, Anchoring ultra-small TiO$_2$ quantum dots onto ultra-thin and large-sized Mxene nanosheets for highly efficient photocatalytic water splitting, Ceram. Int. 47 (2021) 21769–21776, https://doi.org/10.1016/j.ceramint.2021.04.192.

[14] Y. Liu, Z. Hu, J.C. Yu, Photocatalytic degradation of ibuprofen on S-doped BiOBr, Chemosphere 278 (2021), 130376, https://doi.org/10.1016/j.chemosphere.2021.130376.

[15] A.H. Reshak, S. Auluck, Dispersion of the linear and nonlinear optical susceptibilities of Bismuth subcarbonate Bi$_2$O$_2$CO$_3$: DFT calculations, Opt. Mater. 38 (2014) 80–86, https://doi.org/10.1016/j.optmat.2014.09.032.

[16] Y. Fu, M. Zhang, P. Wang, Y. Zhang, C. Xu, Q. Yan, Constructing a Z-scheme 3D hollow pineal-like AgBr/Bi$_2$O$_2$CO$_3$ hybrid material based on ameliorated p-n heterostructure towards exorbitant photocatalytic performance, J. Alloy. Compd. 861 (2020), 157944, https://doi.org/10.1016/j.jallcom.2020.157944.

[17] J. Li, X. Wu, Z. Wan, H. Chen, G. Zhang, Full spectrum light driven photocatalytic in-situ epitaxy of one-unit-cell Bi$_2$O$_2$CO$_3$ layers on Bi$_2$O$_4$ nanocrystals for highly efficient photocatalysis and mechanism unveiling, Appl. Catal. B: Environ. 243 (2019) 667–677, https://doi.org/10.1016/j.apcatb.2018.10.067.

[18] H. Cheng, B. Huang, K. Yang, Z. Wang, X. Qin, X. Zhang, Y. Dai, Facile template-free synthesis of Bi$_2$O$_2$CO$_3$ hierarchical microflowers and their associated photocatalytic activity, ChemPhysChem 11 (2010) 2167–2173, https://doi.org/10.1002/cphc.200901017.

[19] L. Chen, R. Huang, S.-F. Yin, S.-L. Luo, C.-T. Au, Flower-like Bi$_2$O$_2$CO$_3$: Facile synthesis and their photocatalytic application in treatment of dye-containing wastewater, Chem. Eng. J. 193–194 (2012) 123–130, https://doi.org/10.1016/j.cej.2012.04.023.

[20] Y. Liu, Z. Wang, B. Huang, K. Yang, X. Zhang, X. Qin, Y. Dai, Preparation, electronic structure, and photocatalytic properties of Bi$_2$O$_2$CO$_3$ nanosheet, Appl. Surf. Sci. 257 (2010) 172–175, https://doi.org/10.1016/j.apsusc.2010.06.058.

[21] X. Zhang, Q. Wang, J.-W. Hu, L.-H. Zou, J.-W. You, Effect of Ag nanoparticles deposition on photocatalytic activity of Ag_2SO_3, Mater. Res. Bull. 75 (2016) 13–16, https://doi.org/10.1016/j.materresbull.2015.11.019.

[22] T. Soltani, B.-K. Lee, Enhanced formation of sulfate radicals by metal-doped $BiFeO_3$ under visible light for improving photo-Fenton catalytic degradation of 2-chlorophenol, Chem. Eng. J. 313 (2017) 1258–1268, https://doi.org/10.1016/j.cej.2016.11.016.

[23] C.-Y. Wang, Y.-J. Zhang, W.-K. Wang, D.-N. Pei, G.-X. Huang, J.-J. Chen, X. Zhang, H.-Q. Yu, Enhanced photocatalytic degradation of bisphenol A by Co-doped BiOCl nanosheets under visible light irradiation, Appl. Catal. B: Environ. 221 (2018) 320–328, https://doi.org/10.1016/j.apcatb.2017.09.036.

[24] A. Ananth, Y.S. Mok, Synthesis of RuO_2 nanomaterials under dielectric barrier discharge plasma at atmospheric pressure – influence of substrates on the morphology and application, Chem. Eng. J. 239 (2014) 290–298, https://doi.org/10.1016/j.cej.2013.11.036.

[25] Y. Ling, Y. Dai, Direct Z-scheme hierarchical $WO_3/BiOBr$ with enhanced photocatalytic degradation performance under visible light, Appl. Surf. Sci. 509 (2020), 145201, https://doi.org/10.1016/j.apsusc.2019.145201.

[26] J. Di, Z. Xia, H. Li, S. Guo, S. Dai, Bismuth oxyhalide layered materials for energy and environmental applications, Nano Energy 41 (2017) 172–192, https://doi.org/10.1016/j.nanoen.2017.09.008.

[27] X. Zhang, T. Guo, X. Wang, Y. Wang, C. Fan, H. Zhang, Facile composition-controlled preparation and photocatalytic application of $BiOCl/Bi_2O_2CO_3$ nanosheets, Appl. Catal. B: Environ. 150–151 (2014) 486–495, https://doi.org/10.1016/j.apcatb.2013.12.054.

[28] W. Hou, H. Xu, Y. Cai, Z. Zou, D. Li, D. Xia, Precisely control interface OVs concentration for enhance 0D/2D $Bi_2O_2CO_3/BiOCl$ photocatalytic performance, Appl. Surf. Sci. 530 (2020), 147218, https://doi.org/10.1016/j.apsusc.2020.147218.

[29] F. Dong, T. Xiong, Y. Sun, Z. Zhao, Y. Zhou, X. Feng, Z. Wu, A semimetal bismuth element as a direct plasmonic photocatalyst, Chem. Commun. 50 (2014) 10386–10389, https://doi.org/10.1039/C4CC02724H.

[30] H. Zhou, S. Zhong, M. Shen, J. Hou, W. Chen, Formamide-assisted one-pot synthesis of a $Bi/Bi_2O_2CO_3$ heterojunction photocatalyst with enhanced photocatalytic activity, J. Alloy. Compd. 769 (2018) 301–310, https://doi.org/10.1016/j.jallcom.2018.08.007.

[31] Y. Huang, H. Xu, D. Luo, Y. Zhao, Y. Fang, Y. Wei, L. Fan, J. Wu, Facile in situ synthesis of Ag and Bi co-decorated BiOCl heterojunction with high photocatalytic performance over the full solar spectrum, Solid State Sci. 89 (2019) 74–84, https://doi.org/10.1016/j.solidstatesciences.2018.12.017.

[32] Q. Wu, S. Chai, H. Yang, Z. Gao, R. Zhang, L. Wang, L. Kang, Enhancing visible-light driven photocatalytic performance of BiOBr by self-doping and in-situ deposition strategy: a synergistic effect between Bi^{5+} and metallic Bi, Sep. Purif. Technol. 253 (2020), 117388, https://doi.org/10.1016/j.seppur.2020.117388.

[33] B. Dai, A. Zhang, Z. Liu, T. Wang, C. Li, C. Zhang, H. Li, Z. Liu, X. Zhang, Facile synthesis of metallic Bi deposited BiOI composites with the aid of EDTA-2Na for highly efficient Hg^0 removal, Catal. Commun. 121 (2019) 53–56, https://doi.org/10.1016/j.catcom.2018.12.017.

[34] X. Wu, Y. Zhang, K. Wang, S. Zhang, X. Qu, L. Shi, F. Du, In-situ construction of Bi/defective Bi_4NbO_8Cl for non-noble metal based Mott-Schottky photocatalysts towards organic pollutants removal, J. Hazard. Mater. 393 (2020), 122408, https://doi.org/10.1016/j.jhazmat.2020.122408.

[35] F. Chang, B. Lei, X. Zhang, Q. Xu, H. Chen, B. Deng, X. Hu, The reinforced photocatalytic performance of binary-phased composites $Bi-Bi_{12}O_{17}Cl_2$ fabricated by a facile chemical reduction protocol, Colloids Surf. A 572 (2019) 290–298, https://doi.org/10.1016/j.colsurfa.2019.04.014.

[36] W. He, Y. Sun, G. Jiang, H. Huang, X. Zhang, F. Dong, Activation of amorphous Bi_2WO_6 with synchronous Bi metal and Bi_2O_3 coupling: photocatalysis mechanism and reaction pathway, Appl. Catal. B: Environ. 232 (2018) 340–347, https://doi.org/10.1016/j.apcatb.2018.03.047.

[37] W. He, Y. Sun, G. Jiang, Y. Li, X. Zhang, Y. Zhang, Y. Zhou, F. Dong, Defective Bi_4MoO_9/Bi metal core/shell heterostructure: enhanced visible light photocatalysis and reaction mechanism, Appl. Catal. B: Environ. 239 (2018) 619–627, https://doi.org/10.1016/j.apcatb.2018.08.064.

[38] D. Zhang, G. Tan, M. Wang, B. Li, M. Dang, H. Ren, A. Xia, The enhanced photocatalytic activity of Ag-OVs-(001) BiOCl by separating secondary excitons under double SPR effects, Appl. Surf. Sci. 526 (2020), 146689, https://doi.org/10.1016/j.apsusc.2020.146689.

[39] L. Yu, X. Zhang, G. Li, Y. Cao, Y. Shao, D. Li, Highly efficient $Bi_2O_2CO_3/BiOCl$ photocatalyst based on heterojunction with enhanced dye-sensitization under visible light, Appl. Catal. B: Environ. 187 (2016) 301–309, https://doi.org/10.1016/j.apcatb.2016.01.045.

[40] Q. Zhu, W.-S. Wang, L. Lin, G.-Q. Gao, H.-L. Guo, H. Du, A.-W. Xu, Facile synthesis of the novel $Ag_3VO_4/AgBr/Ag$ plasmonic photocatalyst with enhanced photocatalytic activity and stability, J. Phys. Chem. C 117 (2013) 5894–5900, https://doi.org/10.1021/jp400842r.

[41] Z. Qiang, X. Liu, F. Li, T. Li, M. Zhang, H. Singh, M. Huttula, W. Cao, Iodine doped Z-scheme $Bi_2O_2CO_3/Bi_2WO_6$ photocatalysts: facile synthesis, efficient visible light photocatalysis, and photocatalytic mechanism, Chem. Eng. J. 403 (2021) 126327, https://doi.org/10.1016/j.cej.2020.126327.

[42] S. Xiao, Y. Li, J. Hu, H. Li, X. Zhang, L. Liu, J. Lian, One-step synthesis of nanostructured $Bi-Bi_2O_2CO_3-ZnO$ composites with enhanced photocatalytic performance, CrystEngComm 17 (2015) 3809–3819, https://doi.org/10.1039/C5CE00338E.

[43] G. Zhu, S. Li, J. Gao, F. Zhang, C. Liu, Q. Wang, M. Hojamberdiev, Constructing a 2D/2D $Bi_2O_2CO_3/Bi_4O_5Br_2$ heterostructure as a direct Z-scheme photocatalyst with enhanced photocatalytic activity for NOx removal, Appl. Surf. Sci. 493 (2019) 913–925, https://doi.org/10.1016/j.apsusc.2019.07.119.

[44] Y. Lan, Z. Li, W. Xie, D. Li, G. Yan, S. Guo, C. Pan, J. Wu, In situ fabrication of I-doped $Bi_2O_2CO_3/g-C_3N_4$ heterojunctions for enhanced photodegradation activity under visible light, J. Hazard. Mater. 385 (2020), 121622, https://doi.org/10.1016/j.jhazmat.2019.121622.

[45] Y. Li, L. Ding, Z. Liang, Y. Xue, H. Cui, J. Tian, Synergetic effect of defects rich MoS_2 and Ti_3C_2 MXene as cocatalysts for enhanced photocatalytic H_2 production activity of TiO_2, Chem. Eng. J. 383 (2020), 123178, https://doi.org/10.1016/j.cej.2019.123178.

[46] S.V.P. Vattikuti, J. Shim, C. Byon, 1D Bi_2S_3 nanorod/2D e-WS_2 nanosheet heterojunction photocatalyst for enhanced photocatalytic activity, J. Solid State Chem. 258 (2018) 526–535, https://doi.org/10.1016/j.jssc.2017.11.017.

[47] J. Wang, Y. Wang, C. Cao, Y. Zhang, Y. Zhang, L. Zhu, Decomposition of highly persistent perfluorooctanoic acid by hollow Bi/BiOI1-xFx: synergistic effects of surface plasmon resonance and modified band structures, J. Hazard. Mater. 402 (2021), 123459, https://doi.org/10.1016/j.jhazmat.2020.123459.

[48] M. Jahdi, S.B. Mishra, E.N. Nxumalo, S.D. Mhlanga, A.K. Mishra, Smart pathways for the photocatalytic degradation of sulfamethoxazole drug using F-Pd co-doped TiO_2 nanocomposites, Appl. Catal. B: Environ. 267 (2020), 118716, https://doi.org/10.1016/j.apcatb.2020.118716.

[49] A. Verma, S. Kumar, Y.-P. Fu, A ternary-hybrid as efficiently photocatalytic antibiotic degradation and electrochemical pollutant detection, Chem. Eng. J. 408 (2021), 127290, https://doi.org/10.1016/j.cej.2020.127290.

[50] M.N. Chong, B. Jin, C.W.K. Chow, C. Saint, Recent developments in photocatalytic water treatment technology: a review, Water Res. 44 (2010) 2997–3027, https://doi.org/10.1016/j.watres.2010.02.039.

[51] H. Yi, M. Yan, D. Huang, G. Zeng, C. Lai, M. Li, X. Huo, L. Qin, S. Liu, X. Liu, B. Li, H. Wang, M. Shen, Y. Fu, X. Guo, Synergistic effect of artificial enzyme and 2D nano-structured Bi_2WO_6 for eco-friendly and efficient biomimetic photocatalysis, Appl. Catal. B: Environ. 250 (2019) 52–62, https://doi.org/10.1016/j.apcatb.2019.03.008.

[52] T. Yang, J. Peng, Y. Zheng, X. He, Y. Hou, L. Wu, X. Fu, Enhanced photocatalytic ozonation degradation of organic pollutants by ZnO modified TiO_2 nanocomposites, Appl. Catal. B: Environ. 221 (2018) 223–234, https://doi.org/10.1016/j.apcatb.2017.09.025.

[53] H. Gao, S. Yan, J. Wang, Z. Zou, Inorganic ions promoted photocatalysis based on polymer photocatalyst, Appl. Catal. B: Environ. 158–159 (2014) 321–328, https://doi.org/10.1016/j.apcatb.2014.04.036.

[54] X. Liu, D. Xu, D. Zhang, G. Zhang, L. Zhang, Superior performance of 3 D Co-Ni bimetallic oxides for catalytic degradation of organic dye: investigation on the effect of catalyst morphology and catalytic mechanism, Appl. Catal. B: Environ. 186 (2016) 193–203, https://doi.org/10.1016/j.apcatb.2016.01.005.

[55] Z. Wu, Y. Wang, Z. Xiong, Z. Ao, S. Pu, G. Yao, B. Lai, Core-shell magnetic $Fe_3O_4@Zn/Co-ZIFs$ to activate peroxymonosulfate for highly efficient degradation of carbamazepine, Appl. Catal. B: Environ. 277 (2020), 119136, https://doi.org/10.1016/j.apcatb.2020.119136.

[56] X. Xu, L. Meng, J. Luo, M. Zhang, Y. Wang, Y. Dai, C. Sun, Z. Wang, S. Yang, H. He, S. Wang, Self-assembled ultrathin CoO/Bi quantum dots/defective Bi_2MoO_6 hollow Z-scheme heterojunction for visible light-driven degradation of diazinon in water matrix: intermediate toxicity and photocatalytic mechanism, Appl. Catal. B: Environ. 293 (2021), 120231, https://doi.org/10.1016/j.apcatb.2021.120231.

[57] Q. Shen, L. Wei, R. Bibi, K. Wang, D. Hao, J. Zhou, N. Li, Boosting photocatalytic degradation of tetracycline under visible light over hierarchical carbon nitride microrods with carbon vacancies, J. Hazard. Mater. 413 (2021) 125376, https://doi.org/10.1016/j.jhazmat.2021.125376.

[58] S. Perez-Sicairos, K.A. Corrales-Lopez, O.M. Hernandez-Calderon, M.I. Salazar-Gastelum, R.M. Felix-Navarro, Photochemical degradation of nitrobenzene by $S_2O_8^{2-}$ ions and UV radiation, Rev. Int. Contam. Ambient. 32 (2016) 227–236, https://doi.org/10.20937/rica.2016.32.02.08.

[59] Q. Ji, X. Yan, J. Xu, C. Wang, L. Wang, Fabrication of hollow type-II and Z-scheme $In_2O_3/TiO_2/Cu_2O$ photocatalyst based on In-MIL-68 for efficient catalytic degradation of tetracycline, Sep. Purif. Technol. 265 (2021) 118487, https://doi.org/10.1016/j.seppur.2021.118487.

[60] J. Cao, B. Xu, H. Lin, B. Luo, S. Chen, Novel Bi_2S_3-sensitized BiOCl with highly visible light photocatalytic activity for the removal of rhodamine B, Catal. Commun. 26 (2012) 204–208, https://doi.org/10.1016/j.catcom.2012.05.025.

[61] D. Chen, K.P. Taylor, Q. Hall, J.M. Kaplan, The neuropeptides FLP-2 and PDF-1 act in concert to arouse caenorhabditis elegans locomotion, Genetics 204 (2016) 1151–1159, https://doi.org/10.1534/genetics.116.192898.

[62] X. Su, D. Wu, Controllable synthesis of plate BiOBr loaded plate $Bi_2O_2CO_3$ with exposed {001} facets for ciprofloxacin photo-degradation, J. Ind. Eng. Chem. 64 (2018) 256–265, https://doi.org/10.1016/j.jiec.2018.03.023.

[63] Y. Wu, X. Zhao, S. Huang, Y. Li, X. Zhang, G. Zeng, L. Niu, Y. Ling, Y. Zhang, Facile construction of 2D $g-C_3N_4$ supported nanoflower-like $NaBiO_3$ with direct Z-scheme heterojunctions and insight into its photocatalytic degradation of tetracycline, J. Hazard. Mater. 414 (2021), 125547, https://doi.org/10.1016/j.jhazmat.2021.125547.

[64] J. Low, C. Jiang, B. Cheng, S. Wageh, A.A. Al-Ghamdi, J. Yu, A review of direct Z-scheme photocatalysts, Small Methods 1 (2017), 1700080, https://doi.org/10.1002/smtd.201700080.

[65] Z. He, C. Sun, S. Yang, Y. Ding, H. He, Z. Wang, Photocatalytic degradation of rhodamine B by Bi(2)WO(6) with electron accepting agent under microwave irradiation: mechanism and pathway, J. Hazard. Mater. 162 (2009) 1477–1486, https://doi.org/10.1016/j.jhazmat.2008.06.047.

[66] T.S. Natarajan, M. Thomas, K. Natarajan, H.C. Bajaj, R.J. Tayade, Study on UV-LED/TiO$_2$ process for degradation of Rhodamine B dye, Chem. Eng. J. 169 (2011) 126–134, https://doi.org/10.1016/j.cej.2011.02.066.

[67] T.B. Wermuth, S. Arcaro, J. Venturini, T.M. Hubert Ribeiro, A. de Assis Lawisch Rodriguez, E.L. Machado, T. Franco de Oliveira, S.E. Franco de Oliveira, M. N. Baibich, C.P. Bergmann, Microwave-synthesized KNbO$_3$ perovskites: photocatalytic pathway on the degradation of rhodamine B, Ceram. Int. 45 (2019) 24137–24145, https://doi.org/10.1016/j.ceramint.2019.08.122.

[68] T. E, X. Xiao, S. Yang, A new synthesizing method of TiO$_2$ with montmorillonite: effective photoelectron transfer to degrade Rhodamine B, Sep. Purif. Technol. 258 (2021), 118070, https://doi.org/10.1016/j.seppur.2020.118070.

[69] K. Qin, Q. Zhao, H. Yu, X. Xia, J. Li, S. He, L. Wei, T. An, A review of bismuth-based photocatalysts for antibiotic degradation: insight into the photocatalytic degradation performance, pathways and relevant mechanisms, Environ. Res. 199 (2021), 111360, https://doi.org/10.1016/j.envres.2021.111360.